Fault geometry and mechanics of marly carbonate multilayers: an integrated field and laboratory study from the Northern Apennines, Italy

Authors: C. Giorgetti[a,*], C. Collettini[a,b], M.M. Scuderi[a], M.R. Barchi[c] and T. Tesei[b]

Affiliations:
[a] Dipartimento di Scienze della Terra, Università degli Studi La Sapienza, Piazzale Aldo Moro 5, 00185, Rome, Italy.
[b] Istituto Nazionale di Geofisica e Vulcanologia, Via di Vigna Murata 605, 00143 Rome, Italy.
[c] Dipartimento di Fisica e Geologia, Università degli Studi di Perugia, Via Alessandro Pascoli, 06123 Perugia, Italy.

* Corresponding author. Dipartimento di Scienze della Terra Università degli Studi La Sapienza, Piazzale Aldo Moro 5, 00185, Rome, Italy. Tel.: +39 3289106950.
E-mail address: carolina.giorgetti@uniroma1.it

Author's email addresses:
cristiano.collettini@uniroma1.it
marco.scuderi@uniroma1.it
massimiliano.barchi@unipg.it
telemaco.tesei@ingv.it

keywords:
Mechanical multilayer
Northern Apennines
Fault
Rock Mechanics

Abstract

Sealing layers are often represented by sedimentary sequences characterized by alternating strong and weak lithologies. When involved in faulting processes, these mechanically heterogeneous multilayers develop complex fault geometries. Here we investigate fault initiation and evolution within a mechanical multilayer by integrating field observations and rock deformation experiments. Faults initiate with a staircase trajectory that partially reflects the mechanical properties of the involved lithologies, as suggested by our deformation experiments. However, some faults initiating at low angles in calcite-rich layers (θ_i = 5°-20°) and at high angles in clay-rich layers (θ_i = 45°-86°) indicate the important role of structural inheritance at the onset of faulting. With increasing displacement, faults develop well-organized fault cores characterized by a marly, foliated matrix embedding fragments of limestone. The angles of fault reactivation, which concentrate between 30° and 60°, are consistent with the low friction coefficient measured during our experiments on marls (μ_s = 0.39), indicating that clay minerals exert a main control on fault mechanics. Moreover, our integrated analysis suggests that fracturing and faulting are the main mechanisms allowing fluid circulation within the low-permeability multilayer, and that its sealing integrity can be compromised only by the activity of larger faults cutting across its entire thickness.

1. Introduction

The presence of directional heterogeneity (anisotropy) (e.g., *Peacock and Sanderson*, 1992) in sealing layers strongly affects their mechanical and hydrological properties. Low-permeability layers, acting as efficient seals, are often represented by sedimentary sequences characterized by the alternation of weak, clay-rich lithologies, e.g., marl and shale, and strong lithologies, e.g., sandstone and limestone. Directional heterogeneity is possibly associated with mechanical stratigraphy, defined as the presence in a given formation of stratigraphic layers with different mechanical properties (e.g., *Corbett et al.*, 1987; *Wilkins and Gross*, 2002). Within multilayers, these competence contrasts have a key role in fault initiation and growth (e.g., *Peacock and Sanderson*, 1992; *Schöpfer et al.*, 2006; *Schöpfer et al.*, 2007; *Ferrill and Morris*, 2008; *Childs et al.*, 2009; *Roche et al.*, 2012). In the incipient phase, faults hosted in multilayers develop a staircase trajectory with plane refraction at competence contrasts. This staircase trajectory results in a variable fault orientation that can be described by the angle of fault initiation. The angle of fault initiation θ_i is defined as the angle between the maximum principal stress and the fault plane and it depends on the failure strength of the faulted rocks (*Anderson*, 1951). In a mechanical multilayer, the strength heterogeneity results in different θ_i values within each different stratigraphic layer. The overall strength of a layer can also be influenced by the presence of pre-existing cohesionless surfaces, such as joints, that can further deflect the trajectory of the fault and thus change the θ_i value (e.g., *Peacock and Sanderson*, 1992; *Crider and Peacock*, 2004; *Roche et al.*, 2012). Furthermore, an additional directional heterogeneity is related to the intrinsic anisotropy of weak layers, i.e., the planes of weakness resulting from rock foliation (e.g., *Shea and Kronenberg*, 1993; *Massironi et al.*, 2011; *Bistacchi et al.*, 2012; *Misra et al.*, 2015). Deformation experiments on intact rocks show that the orientation of foliation with respect to the maximum principal stress strongly influences the strength of the rocks (e.g., *Jaeger*, 1960; *Donath*, 1961; *Jackson and Dunn*, 1974; *McCabe and Koerner*, 1975, *Bolognesi and Bistacchi*, 2016). Shear fractures in foliated rocks, developed during triaxial experiments, may reactivate the planes of weakness, even when the maximum principal stress is inclined at high angles, such as 45°-60°, to the pre-existing surface (*Donath*, 1961).

In the first stages of growth, slip along staircase faults causes the development of dilational jogs within competent layers (e.g., *Sibson*, 1996). The presence of dilational jogs has strong implications on fluid circulation in low-permeability multilayers, often promoting fluid flow in the direction parallel to the intersection of the fault plane and the bedding (e.g., *Sibson*, 1996; *Ferrill and Morris*, 2003). Structural studies on the distribution of displacement in mechanical multilayers are essential in order to better understand fluid flow properties within fault zones (e.g., *Manzocchi et al.*, 2008; *Childs et al.*, 2009; *Manzocchi et al*., 2010). However, most of the previous field-based studies have only given a detailed geometrical description of complex faults within mechanical multilayers (e.g., *Peacock and Sanderson*, 1992; *Nicol et al.*, 1996; *Gross et al.*, 1997; *Wilkins and Gross*, 2002; *Soliva and Benedicto*, 2005; *Schöpfer et al.*, 2006; *Antonellini et al.*, 2008; *Ferrill and Morris*, 2008; *Childs et al.*, 2009; *Ferrill et al.*, 2011; *Roche et al.*, 2012; *Kristensen et al.*, 2013), while a complementary mechanical characterization is still lacking. In this paper we integrate field observations with rock deformation experiments to investigate fault evolution within a mechanical multilayer consisting of alternating limestones and clay-rich marls. We aim to better characterize the role of mechanical properties on the overall deformation style and fluid circulation.

2. Geological framework

We studied outcrops of faulted multilayers located in the northeastern limb of the Monte Montiego Anticline (Figure 1) in the Umbria-Marche Apennines that represent the outer part of the Northern Apennines (e.g., *Bally et al.*, 1986; *Barchi et al.*, 2012). The Northern Apennines are a complex, arc-shaped fold-and-thrust belt having an overall northeastward convexity and vergence (e.g., *Carmignani et al.*, 2001; *Barchi et al.*, 2001), developed in the framework of the Europe-Africa convergence (e.g., *Reutter et al.*, 1980; *Alvarez*, 1991; *Doglioni et al.*, 1998; *Carminati and Doglioni*, 2012). The Umbria-Marche Apennines are characterized by large asymmetric anticlines overturned eastward on tight synclines with fold axes trending NW-SE (e.g., *Abbate et al.*, 1970; *Lavecchia et al.*, 1988). Locally, the Monte Montiego Anticline has a fold axis trending WNW-ESE (*Engelder*, 1984).

The Mesozoic carbonates are folded coherently with the compressional regime and they are also affected by small-scale faulting. Specifically, we studied mesoscale faults showing subvertical dips with displacements ranging from less than 1 cm up to ~20 m. Kinematic indicators, i.e., bedding offsets, drag folds, and subhorizontal slickenfibers, indicate a strike-slip movement. The relationship of fault-bedding intersections and the sense of displacement are consistent with fold-axis-parallel extension (e.g., *Marshak et al.*, 1982). Strike-slip faults are commonly found in fold-and-thrust belts (e.g., *Sylvester*, 1988; *Hindle and Burkhard*, 1999), including the anticlines of the Umbria-Marche Apennines (e.g., *Marshak et al.*, 1982; *Barchi et al.*, 1993). Moreover, a previous study (*Marshak et al.*, 1982) in the same area of the Apennines proposed that the activity of strike-slip faults is, at least in part, contemporaneous with the formation of the anticline.

The studied faults developed within the Lower Cretaceous Marne a Fucoidi Formation. The lithology of the Marne a Fucoidi Formation is highly variable in terms of composition, with $CaCO_3$ content ranging from 4% to 75% (*Giorgioni et al.*, 2016; *Li et al.*, 2016). The remaining percentage is made of a homogeneous clay mineral assemblage consisting of ~50% smectite, ~30% illite and ~20% mixed layer illite-smectite (*Coccioni et al.*, 1989). The Marne a Fucoidi Formation is also highly variable in terms of thickness and spacing of competent limestone layers (e.g., *Tonarghi et al.*, 1989; *Coccioni et al.*, 1989). The high lithological variability of this formation results in high variability of mechanical properties, thus defining mechanical multilayers, prone to develop complex fault geometries. Despite this high variability, the alternation of layers with higher and lower $CaCO_3$ content is always evident. In the present work, we define competent layers as those characterized by relatively high $CaCO_3$ content and incompetent layers as those characterized by low $CaCO_3$ content and the presence of sedimentary foliation.

3. Investigation methods

3.1. Theoretical framework for field observations

We studied the along-strike geometry of outcropping faults with increasing displacement from less than one centimeter to a few meters in order to reconstruct the initiation and early stages of faulting. Additionally, we studied a single fault with an apparent displacement (separation) of about 20 m to evaluate a more mature fault stage.

The mechanical characterization of the mapped faults is based on geometrical relationships between the slipping surfaces and the local stress field orientation. Fault initiation can be evaluated by using the Coulomb failure criterion (*Coulomb*, 1776):

$$\tau = c + \mu_i(\sigma_n - P_f) \tag{1}$$

where τ is the shear stress, σ_n is the normal stress on the failure plane, P_f is the fluid pressure, c is the cohesive strength and μ_i is the internal friction of the intact rock. The angle θ_i between the fault and the maximum principal stress σ_1 is defined as (e.g., *Anderson*, 1951; *Mandl*, 1988)

$$\theta_i = 45 - \frac{\varphi_i}{2} \tag{2}$$

where φ_i is the angle of internal friction, related to μ_i through the relation $\mu_i = \tan \varphi_i$. Amontons' law defines the shear stress necessary to reactivate a pre-existing, cohesionless fault (e.g., *Jaeger and Cook*, 1979) as follows:

$$\tau = \mu_s(\sigma_n - P_f) \tag{3}$$

where μ_s is the coefficient of sliding friction of the surface. The angle between the fault and the maximum principal stress σ_1 is defined as the angle of fault reactivation, θ_r.

We used both the geometry and the kinematics of the mapped faults to reconstruct the orientation of the stress field. The kinematic analysis was conducted through the linked Bingham distribution method (*Marrett and Allmendinger*, 1990), using all the calcite slickenfibers and striae with a strike-slip component (rakes <45°). Assuming a pure shear deformation, the resulting strain axes can be considered parallel to the stress axes. The pure shear assumption is reasonable for the studied outcrops since the fault system is characterized by small conjugate strike-slip faults occurring in a tectonic regime of shortening (e.g., *Sylvester*, 1988). We also reconstructed the local stress field for each single outcrop considering σ_3 perpendicular to extensional fractures, σ_2 parallel to the intersection of conjugate faults and σ_1 perpendicular to the plane containing σ_2 and σ_3. The direction of σ_2 was further constrained with the hinges of drag folds that, assuming a σ_1 perpendicular to the bedding (e.g., *Ramsay and Huber*, 1987), are parallel to the σ_2.

We used the local stress field of each outcrop to estimate the angle of fault initiation θ_i for small displacement faults, i.e., < 1 cm, whereas the reconstructed "regional" stress field resulting from the linked Bingham distribution method was used to estimate the angles of fault reactivation θ_r for large displacement faults, i.e., > 1 cm. We chose this threshold value because faults with displacement larger than ~1 cm are characterized by different geometry in respect to smaller faults.

3.2 Laboratory investigations

We performed rock deformation experiments on samples collected from the studied outcrops mentioned above, in exposures not affected by faulting. Marl cohesion is significantly lower than limestone cohesion (e.g., *Marinos and Hoek*, 2001) and foliation planes represent surfaces of almost zero cohesion. Thus, we designed experiments in different configurations (Table 1). Intact rock samples were collected from competent layers (~70-80 wt.% of $CaCO_3$, Table 1) to perform triaxial deformation experiments on cylindrical samples. Incohesive rock samples were collected from incompetent marly layers (59 wt.% of $CaCO_3$, Table 1) and powdered to perform biaxial friction experiments. We estimated a $CaCO_3$ content of ~80 wt.% in the competent limestone and ~60 wt.% in the incompetent marl (Table 1). Excluding the samples with chert nodules, the remaining weight reflects the amount of clay minerals, i.e., ~20% in competent limestone and ~40% in incompetent marl. Given the negligible cohesion, we assumed that the maximum shear strength of powdered marl represents a good proxy for strength of the parent intact rock.

Both triaxial and biaxial experiments were performed in a servo-controlled biaxial deformation apparatus installed in the High Pressure-High Temperature Laboratory at the INGV in Rome, Italy (Figure 2). This apparatus is equipped with a pressure vessel, that allows for the application of confining pressure and pore fluid pressure (Figure 2a) (*Collettini et al.*, 2014). Vertical and horizontal loads are controlled and measured using load cells with 0.03 kN accuracy and positioned within the pressure vessel. Vertical and horizontal displacements are controlled and measured through Linear Variable Differential Transducers (LVDTs) sensors with 0.1 μm accuracy. The pressure vessel is equipped with two removable doors, both sealed with O-rings to prevent confining oil leakage. High-pressure ports allow the communication between the sample assembly and up- and down- stream pressure intensifiers (Figure 2a). Similarly, a third pressure intensifier is connected to the pressure vessel to apply confining pressure. Pore fluid pressure is applied using tap water as a fluid and confining pressure via a confining oil, i.e., 13,8660 VE 15–68 Vaselina Enologica (Green Star High Tech lubricant sand additives). Pressure values of the intensifiers are monitored through pressure transducers with 7 kPa accuracy. Displacement values of the intensifiers are monitored using LVDT sensors with 0.1 μm accuracy. Pore pressures and confining pressure are servo-controlled. During each experiment, forces, pressures and displacements were continuously acquired using a 24-bit analog to digital system and recorded at a frequency ranging between 1 - 10 Hz, depending on the loading velocity imposed on the vertical piston.

3.2.1 Triaxial deformation experiments

We conducted triaxial compression experiments on cylindrical samples 38 mm in diameter and 76 mm in length, which were cored from two intact blocks in an orientation perpendicular to the layering. The two intact blocks come from two different competent layers consisting of thinly-bedded marly limestone (72 wt.% and 83 wt.% of $CaCO_3$, Table 1). One of these two blocks contains a level enriched in small chert nodules. To estimate the porosity, our samples were dried for 96 h at a temperature of 60° and then saturated with tap water under vacuum for one week. We calculated the porosity as follows:

$$\phi = \frac{V_p}{V_t} \quad (4)$$

where V_p is the volume of interconnected pores, calculated as the difference in weight between the saturated and dried sample multiplied by the density of water, and V_t is the sample's total volume.

The cylindrical sample was placed in-between two stainless steel end platens, equipped with internal channels for fluid flow (Figure 2b). The sample was jacketed with a poly-olefin heat-shrink tube and sealed with steel wires at the extremities to prevent oil from entering into the sample. The internal channels of the two end platens were connected to two access ports, through pore pressure lines, to allow the application of up- and down-stream pore pressures. We ran three experiments at different values of confining pressure and room temperature for each of the two tested lithologies (details in Table 1). We used the following procedure in all the triaxial experiments. We began by applying a constant confining pressure (P_c), with values of 10, 20 and 30 MPa. Then the differential stress was increased, imposing a constant axial strain rate of 1.3×10^{-6} s^{-1} by moving the vertical piston at a constant displacement rate of 0.1 μm/s. To evaluate fracture-enhanced permeability, we imposed different values of pore pressure between the up- and down- stream ends, i.e., 2 MPa and 1 MPa, respectively. Since the initial porosity of the tested samples was ~4%, as calculated from Equation 4, fluid flow through the samples was observed only after failure when fractures developed from the bottom to the top of the samples. Consequently, we considered pore pressure to be zero ($P_f = 0$) within the sample throughout the experiment.

The axial strain was evaluated after correcting the values of the vertical load point displacement for the machine stiffness on the vertical axis that, depending on the confining pressure, ranged between 791.1 kN/mm and 781.1 kN/mm. The resulting stress field acting on the sample during the experiment consisted of horizontal $\sigma_2 = \sigma_3 = P_c$ and vertical $\sigma_1 = P_c + \sigma_d$, where

σ_d is the differential stress (Figure 2b). The effective mean stress, considering the pore pressure P_f = 0, acting on the sample is given by

$$\sigma_m = \frac{\sigma_1 + 2\sigma_3}{3} \tag{5}$$

In the framework of critical state soil mechanics (e.g., *Schofield and Wroth*, 1968), the peak differential stress shows a positive correlation with the effective mean stress, typical of brittle failure described by a Mohr-Coulomb failure envelope (e.g., *Paterson and Wong*, 2005) that can be fitted by the following linear equation

$$\sigma_d = C + M\sigma_m \tag{6}$$

The parameters of equation 6 are related to the cohesion c and the friction μ_i of the Coulomb failure criterion (Equation 1) as follows (e.g., *Bolton*, 1979)

$$M = \frac{6 \sin \varphi_i}{3 - \sin \varphi_i}; C = \frac{6c \cos \varphi_i}{3 - \sin \varphi_i} \tag{7}$$

Following equations 6, 7 and 2 we estimated and compared the experimentally derived values of θ_i with the values of θ_i measured in the studied outcrops.

3.2.2 Biaxial deformation experiments

We conducted biaxial deformation experiments in a double-direct shear configuration on powders prepared from outcropping marls (59 wt.% of $CaCO_3$, Table 1) that were crushed and sieved to < 125 μm grain size. In this configuration, two layers of powdered marl were sandwiched in a three steel block assembly (Figure 2c). The experiments were run within the pressure vessel to apply confining pressure (*Scuderi and Collettini*, 2016 for additional details). Sintered stainless steel frits were placed within the blocks in contact with the gouge layers to allow homogeneous fluid distribution over the entire area of the sample. To isolate the gouge layers from the confining oil, the sample assembly was jacketed (Figure 2d) as described in the following procedure. First the assembly was covered and taped with a rubber sheet to protect the layers. Then the assembly was covered with two layers of latex tube in order to prevent frits of the central block from cutting the external jackets. Finally the sample assembly was encapsulated within two custom-made latex boots and sealed with steel wires placed where the forcing blocks are equipped with O-rings. The sample assembly, equipped with internal conduits for pore fluids (Figure 2d), was connected, through pore pressure lines, to three access ports to allow for the application of up- and down-stream pore pressures.

We ran two experiments at a confining pressure of 15 MPa (Table 1). One sample was sheared at a normal stress of 20 MPa for ~1.6 cm of displacement. Another experiment was performed shearing the layers at different normal stresses ranging from σ_n = 30 MPa to σ_n = 50 MPa, for a total displacement of ~1.4 cm. We used the same loading procedure in both the experiments, for comparison purposes. We applied and maintained constant confining pressure throughout the experiment. We then applied an additional horizontal force in order to reach the target value of the normal stress. We saturated the sample with tap water applying 10 MPa up-stream pore pressure, leaving the down-stream side open to the atmosphere until flow-through was established. At this stage, in order to achieve fully saturated boundary conditions but at zero pore pressure, for comparison purposes with the triaxial deformation tests, we decreased the upstream pore pressure to zero. We then opened the downstream pore pressure line to the atmosphere in order to perform the experiment in drained conditions. Additional details on the experimental procedure for the double direct shear configuration within the pressure vessel are reported in *Scuderi and Collettini* (2016). Marly powders were sheared at room temperature and at a constant velocity of 10 μm/s.

The displacement values of the vertical and horizontal load points were corrected for the elastic stretch of each load frame, taking into account that the machine stiffness is 1283 kN/mm on the horizontal axis and 928.5 kN/mm on the vertical axis. The average shear strain within the layer was calculated by progressively summing the shear displacement increments divided by the measured layer thickness.

The peak and steady state shear strength were measured for each normal stress and fitted with a linear regression in order to obtain the parameters in the Coulomb failure criterion and in the Amontons' law (Equation 1 and 3), thus obtaining the internal friction μ_i and the sliding friction μ_s.

4. Structural data

In order to characterize different stages of fault evolution and to reconstruct the related stress field, we studied in detail two outcrops. Outcrop A (Figure 3, 302690 N 4830479 E UTM coordinates 33T) is characterized by an overall marl-rich multilayer containing ~3-10 centimeters thick clay-rich layers with a strong primary foliation. These foliated layers alternate with competent limestone layers that are ~ 3-10 centimeters thick. Outcrop B (Figure 4, 302684 N 4830502 E UTM coordinates 33T zone) is characterized by an overall limestone-rich multilayer where competent limestone layers, ~2-5 centimeters thick, alternate with foliated marl layers, ~2-5 centimeters thick. In order to consider a more mature stage of fault evolution, we also studied the largest fault affecting our study area (outcrop C, Figure 7, 302628 N 4830455 E UTM coordinates 33T zone), a left-lateral strike-slip fault with a net displacement of about 20 m.

4.1. Fault architecture: from incipient to "mature" faults

Faults with displacement of ~1 cm or less develop a staircase trajectory with respect to the orientation of bedding, characterized by fault plane refraction at lithological contrasts (Figure 3a-b and 4a-b), as previously described in mechanical multilayers (e.g., *Peacock and Sanderson*, 1992; *Wilkins and Gross*, 2002; *Schöpfer et al.*, 2006; *Ferrill and Morris*, 2003; *Childs et al.*, 2009). Marly layers locally show widespread fractures characterized by conjugate planes with a dihedral angle of ~90° (Figure 5). These small shear fractures, with displacement of a few millimeters, are confined within incompetent layers and often do not show calcite mineralization. Contrastingly, all the faults that crosscut more than a single layer are characterized by calcite mineralization (Figure 5b and 6). Faults across more competent layers develop a few centimeters thick dilational jogs filled with overlapping layers of calcite slickenfibers or blocky calcite (Figure 6a-c; e.g., *Sibson*, 1996; *Ferrill et al.*, 2014). Fault segments running through less competent layers are often marked by calcite veins with a thickness of few millimeters characterized by overlapping layers of slickenfibers (Figure 6d).

With increasing displacement from 1 cm up to 2 m, fault trajectories evolve toward a more straight geometry, with no refraction at competence contrasts at the level of the single bed. Moreover, the fault zones widen up to 10-20 cm in thickness (Figure 3c-d and 4c-d). Within clay-rich layers, faults tend to partition deformation through the development of numerous splays that ramp through the sedimentary succession (Figure 3a and 4a). Within competent layers, faults cut and rework dilational jogs (Figure 4c) and occasionally contain cataclastic breccias characterized by angular clasts of micritic limestone supported by calcite cement (Figure 6e). Faults with ~1-2 m of displacement develop foliated fault cores with a width of 10-20 cm, in which small sigmoidal duplexes of competent limestone are embedded in a marly matrix derived from incompetent layers (Figure 3d and 4d). Slipping surfaces occurring within fault cores are often marked by slickenfibers. The width of the fault cores varies along the fault structure depending on the displacement, lithology, spacing and thickness of the competent layers. Where marly layers are predominant, the deformation appears localized within a thin fault core, i.e., ~1-2 cm thick; where thick competent layers are closely spaced, the fault core is 10-20 cm thick and well-developed. The main left-lateral fault in Figure 3a has a thin fault zone through the reddish marl, whereas it develops a thicker fault zone cutting across limestone layers (Figure 3d). Moreover, the straightness of fault trajectory depends on the amount of displacement and on the scale of the anisotropy: fault trajectory is insensitive to competence contrasts between layers whose thickness is well below the displacement, but it is still sensitive to competence contrasts between different groups of layers. As an example, the trajectory of the main left-lateral fault in Figure 3a, that accumulates ~1 m of displacement, is insensitive to anisotropy due to marl-limestone alternation but it is sensitive to the anisotropy of groups of layers since the fault plane refracts at the boundary between the reddish and the greyish brown group of layers resulting in a trajectory deflection of ~13°.

The more mature fault zone observed in the studied outcrops accumulated about 20 m of displacement (Figure 7). This fault shows an overall straight trajectory and a wide, up to 45 cm, well-organized foliated fault core, characterized by a SCC' fabric (*Koopman*, 1983) in which a well-developed marly foliation embeds sigmoidal fragments of limestone, up to ~10-20 cm long and a few centimeters thick (Figure 7b-c). Despite the slip surface trajectory is relatively straight, the boundaries of the fault zone preserve a staircase shape, likely inherited from the early stages of the fault activity. This structure results in a variable thickness of the fault rock, ranging from 5 to 45 cm (Figure 7c). The fault rock is not equally derived from the two blocks involved in the faulting processes. Most of the fault rock consists of reddish marl from the marl-rich group of layers in the hanging-wall (unit A, Figure 7), whereas only a thin layer of fault rock, ~ 1 cm thick, derives from the limestone-rich group of layers in the foot-wall block (unit B, Figure 7). This thin layer consists of an ultracataclasite mainly developed along boundary shear planes (C plane in Figure 7b). The rocks surrounding the fault are intensely deformed: in unit A the deformation is localized along antithetic faults that merge into the main fault zone, whereas unit B is mainly affected by a more distributed fracturing. The observed preservation of the staircase trajectory at the boundary of mature fault cores (Figure 4d and 7c) suggest a mechanism that deactivates the slipping surfaces in between the two steps developing a straight surface immediately next to them, causing progressive strain localization in the fault core. The strong asymmetry of deformation in Unit A and Unit B in proximity of the more mature fault zone (Figure 7) implies that, starting from a staircase trajectory in the more competent Unit B, where the boundary is sharp (Figure 7c), the fault growth propagates within the less competent Unit A producing a wide damage zone (e.g., *Ferrill et al.*, 2011; *Ferrill et al.*, 2012).

4.2. Stress field orientation and angles of faulting

The reconstructed “regional” stress field results in a N-S trending subhorizontal σ_1, an E-W trending subhorizontal σ_3 and a subvertical σ_2 (Figure 8a). The resulting maximum principal stress σ_1 (N5°E) is slightly rotated with respect to the direction of maximum compression that generated the compressional structures of the area (N22°E-N29°E, *Marshak*, 1982; *Engelde*r, 1984). The orientation of the local stress fields in general is consistent with the regional stress field obtained from slickenfibers and striae (Figure 8a).

The frequency of θ_i values is bimodal and controlled by lithology (Figure 8b). In limestone layers the angle of fault initiation ranges between θ_i = 5° and θ_i = 28°, whereas in marl layers it ranges between θ_i = 32° and θ_i = 86°. Most of the angles of fault initiation concentrate between θ_i = 20° and θ_i = 30° in competent layers and between θ_i = 40° and θ_i = 60° in incompetent layers. After the incipient stage, faults show reactivation angles ranging between θ_r = 17° and θ_r = 72°. The frequency of θ_r values shows a unimodal distribution centered at θ_r = 50°- 60° (Figure 8b).

5. Laboratory rock deformation data

5.1. Strength and fracture permeability of cohesive limestones

Figure 9a shows the evolution of differential stress, σ_d, with increasing axial strain ε_a. For each experiment, differential stress increases linearly until a peak stress, followed by a stress drop. This evolution is consistent with a brittle faulting regime (e.g., *Paterson and Wong*, 2005; *Wong at al*., 1997) and confirmed by the localization of deformation along crosscutting sharp fractures in the tested samples (e.g., Figure 10b). With increasing confining pressure from 10 to 30 MPa, both differential stress at failure and residual differential stress increase for all the tested samples. Conversely, the stress drop progressively decreases and requires more strain from the peak to the steady-state value. Samples with chert nodules show higher values of peak differential stress, σ_d, when the forming fracture cuts across the nodules, i.e., P_c = 10 and 20 MPa. At P_c = 30 MPa the values from different samples overlap. The analysis of the chert-rich sample deformed at P_c = 30

MPa show that the fracture does not pass through the nodules, suggesting that the resulting strength represents the marly limestone strength, and can be therefore compared with the strength of the chert-free samples. Thus, excluding samples whose fractures cut across chert nodules (chert-rich samples at P_c = 10 and 20 MPa), the peak stress values in a σ_d versus σ_m space (Figure 9b) are well fitted with a linear regression of the form of Equation 6 that results in M values of 1.54 and C values of 66 MPa. Following Equation 7, we obtain internal friction μ_i = 0.78 and cohesion c = 33 MPa and using Equation 2 we derive experimentally the angle of fault initiation θ_i = 26°.

During the triaxial tests, although we imposed a pore fluid pressure gradient of 1 MPa, we did not observe any significant fluid flow during loading of the sample (Figure 10a). We observe significant fracture enhanced permeability in only one experiment at 10 MPa confining pressure (Figure 10). The analysis of the samples at the end of the experiments confirms that this is the only sample developing a through-going fracture, providing a path for fluid flow (Figure 10b). Since during failure the pore pressure at the bottom of the sample increases to re-equilibrate with the pore pressure at the top of the sample, we have a fluid flow controlled by a differential gradient of pore pressure changing with time. The permeability also varies with time due to the ongoing deformation. On the basis of this consideration, in order to estimate the enhanced fracture permeability k we applied Darcy's Law:

$$k = \frac{Q\,\eta\,dl}{A\,dP_p} \tag{8}$$

considering the current flow rate Q equal to the derivative of the fluid volume curve with time, the current length of the cylindrical sample dl, and the current differential pore pressure dP_p. A is the cross-sectional area of the cylindrical sample and η is the viscosity of the water, that is assumed to be 1.002×10^{-9} MPa s^{-1}. The estimated dynamic permeability, due to fracturing, ranges between k = 2.7×10^{-16} m^2 and $k = 5.6 \times 10^{-16}$ m^2.

5.2. Strength of incohesive marls

The evolution of the shear stress, τ, with increasing shear strain, γ, during friction experiments (Figure 11a) shows an initial increase until the attainment of peak strength, followed by a decay to a steady-state strength. With increasing normal stresses from 20 to 50 MPa, the shear strength of marls increases, as well as the difference between the peak strength and the following steady state strength (Figure 11b). The values of peak and steady-state shear strength show a linear dependence with normal stress indicating brittle deformation. Assuming zero cohesion, the envelope of peak shear stresses results in friction μ_i = 0.42, whereas the envelope of steady-state strength results in lower friction μ_s = 0.39 (Figure 11b). We used these values of μ_i and μ_s to estimate the angle of fault initiation and the optimum angle for fault frictional reactivation respectively. Due to the small difference between μ_i and μ_s from Equation 2 results that the optimum angles for fault initiation, θ_i, and reactivation, θ_r, are similar, i.e., ~34°.

6. Discussion

6.1. Fault initiation

6.1.1 Fault initiation in limestone

The angle of fault initiation derived from laboratory experiments on limestones, i.e., θ_i = 26°, is consistent with the peak of the distribution of faults within competent layers, i.e., 20° < θ_i < 30° (Figure 8b). This correspondence indicates that the geometry of faults developing at this θ_i is controlled by rock strength. In limestone layers, faults occasionally reactivate joints and extensional fractures formed almost parallel to σ_1, developing θ_i of 5° (e.g., histogram in Figure 8b). The propagation of fault segments through pre-existing fractures in limestone beds has been already well documented in mechanical multilayers (e.g., *Wilkins et al.*, 2001; *Crider and Peacock*, 2004; *Roche et al*., 2012). Considering pre-existing surfaces with no cohesion and on the grounds of our laboratory results, we suggest that the variability of θ_i observed in outcropping limestones likely result from the contemporaneous development of new shear fractures, i.e., θ_i ranging between 20°

and 30°, and reactivation of pre-existing cohesionless surfaces, i.e., θ_i ranging between 0° and 20° (Figure 12a). An additional mechanism able to explain values of $\theta_i \approx 20°$ is the occurrence of hybrid extensional shear fractures (e.g., *Ramsey and Chester*, 2004) favored by fluid overpressure (Figure 12b). Assuming a low value of the minimum effective principal stress, local variations of the principal stresses, due possibly to the difference in elastic and poroelastic properties of the layers (e.g., *Gross*, 1995; *Healy*, 2009), can result in the simultaneous development of shear and hybrid fractures. Previous studies have proposed the occurrence of hybrid fractures as a key factor in controlling fault trajectory in mechanical multilayers (e.g., *Ferrill and Morris*, 2003; *Ferrill et al.*, 2012). In the studied faults the occurrence of hybrid fractures is supported by the field observation that re-precipitated calcite within some dilational jogs has a growth direction that is not perpendicular to the wall of the fracture (Figure 6b) (e.g., *Price and Cosgrove*, 1990). However, the limited evidences collected in the field suggest that this is not the dominant mechanism.

6.1.2 Fault initiation in marls

The strength of marls, μ_i = 0.42, results in θ_i of 34°, that is at the bottom of the estimated range (32°-86°) of mapped faults (Figure 8b). Therefore, most of θ_i values cannot be explained by the Coulomb failure criterion for fault initiation (Equation 1 and 2). Indeed, through less competent clay-rich layers faults tend to form at high angles to σ_1, and even parallel to the layering (Figure 4a-b), due to the strong anisotropy of these clay-rich layers. Previous field observations have reported that fault segments propagate parallel to the layering in weak lithologies being discouraged to propagate within the bounding stronger layers (*Roche et al.*, 2012). However, fault initiation at angles higher than 45° requires not only a weak lithology but also the possibility to reactivate pre-existing discontinuities. We propose that the primary foliation of the marls, characterized by weak clay-rich layers, provides favorable horizons able to deviate fault trajectory, as in part suggested in previous studies (e.g., *Jaeger*, 1960; *Donath*, 1961; *Shea and Kronenberg*, 1993; *Bistacchi et al.*, 2012; *Misra et al.*, 2015). In the field we observe that the maximum value of θ_i is limited by the angle between foliation and σ_1. The maximum θ_i is ~86° in outcrop B where σ_1 is almost perpendicular to the layering (Figure 4a) and ~46° in outcrop A where σ_1 is on average at 52° to the layering (Figure 3a).

6.1.3 Fault initiation in the mechanical multilayer

The intense fracturing that characterizes the marls, bounded by unbroken limestone beds, suggests that the onset of inelastic deformation occurs within incompetent layers (Figure 5a). At an incipient stage of deformation, before the localization along a fault plane crosscutting different layers, clay-rich layers achieve the yield strength and deform inelastically. At the same time, under the same stress field, limestone layers still have an elastic behavior. These limestone layers consist of micrite and have low porosity (~4%) and low permeability, as indicated by laboratory experiments (Figure 10). Moreover, we suggest that previous fractures related to folding do not significantly increase limestone permeability, since in the field we observe that extensional fractures are sealed by calcite cement. The inelastic deformation within marly layers thus occurs under undrained conditions (e.g., *Rice*, 1975; *Rudnicki and Rice*, 1975; *Rudnicki*, 1984). If the fluid and the rock are both considered incompressible, the undrained response is also incompressible and any stress increment is exactly compensated by changes in pore pressure, so that the strength is pressure insensitive (*Rudnicki*, 2002). The initial failure thus localizes at 45° to the maximum principal stress (*Runesson et al.*, 1996; *Rudnicki*, 2002), as supported by the strong fracturing confined within marly layers showing a pattern characterized by the development of conjugate shear fractures with a dihedral angle of 90° (Figure 5a). Because the marly layers are characterized by a pressure-insensitive behavior and do not allow for stress drop, any stress increments within the multilayer will result in an increase of differential stress within the limestone layers. The differential stress thus increases until the achievement of the limestone strength, resulting in the propagation of a fault within the multilayer and allowing for fluid drainage (Figure 5b).

6.2. Fault growth and angles of fault reactivation

With accumulating displacement the fault core progressively develops a well-organized marly foliation embedding fragments of limestone. With accumulating slip faults cut across dilational jogs causing fault straightening and rotation. Therefore the angle of fault reactivation, θ_r, in general increases with displacement. For example, in outcrop A (Figure 3) the asymmetry of the fault system with respect to σ_1 results from the different amount of displacement accumulated by the faults. Here, the main left-lateral fault has accumulated ~1 m of displacement and shows a θ_r angle of about 43°. The conjugate dextral faults, characterized by lower displacements, depict θ_r in the range of 30°-42° due to small-scale anisotropies produced by the limestone-marl alternation. Other structural anisotropies such us pre-existing joints and extensional veins control θ_r values during the very initial stages of faulting, whereas the influence of foliation is persistent up to higher displacement. For faults with displacement in the range of ~10 cm ~1 m, the dihedral angle is high since the influence of marly foliation in flattening fault planes is more efficient. A representative example is depicted by the conjugate faults of outcrop B (Figure 4) showing high θ_r angles, i.e., $55° < \theta_r < 68°$, with frequent layer parallel fault segments. For further displacement (1 - 2 m) we document θ_r of about 42° in both marly and limestone-rich outcrops (Figure 3d and 4d). These faults display a foliated fault core, suggesting that the slip is mainly accommodated within the clay matrix, and therefore clay friction controls θ_r. The mature fault (Figure 7) characterized by a θ_r of about 50°, further supports the idea that after the achievement of a well-organized clay-rich fault structure, the orientation of the fault does not change significantly.

In summary, our field analysis suggests that the geometry of a fault is influenced by anisotropies having the same or higher scale than fault displacement: 1) a small fault, with ~1 cm of displacement, refracts at the competence contrasts between marly and limestone layers; 2) a fault, with ~1 - 2 m of displacement, refracts at competence contrast between different groups of layers and 3) a large displacement fault refracts due to the competent contrast of the different formations, i.e., between the Marne a Fucoidi Formation and the Maiolica Formation.

Based on the field observation that fault cores are foliated, localizing slip within the clay-rich matrix, we consider the steady-state friction value of the powdered marl (cf. paragraph 5.2 and Figure 11b) as a good approximation for the frictional strength of the outcropping faults. Experiments on natural fault rock samples indicate that the development of a through-going phyllosilicate-rich network is one of the primary mechanisms for fault weakening (e.g., *Holdsworth* 2004; *Collettini et al.*, 2009; *Carpenter et al.*, 2011; *Tesei et al.*, 2014; 2015). The coefficients of sliding friction observed during our saturated experiments containing 40% of clay, μ_p = 0.39 - 0.43 and μ_{ss} = 0.38 - 0.41, are in good agreement with previous laboratory studies on mixtures of weak clay and strong minerals characterized by a similar percentage of clay (*Tembe et al.*, 2010).

We compare our values of θ_r measured in the field with *frictional* fault reactivation theory using the equation (*Sibson*, 1985):

$$R = \frac{\sigma_1}{\sigma_3} = \frac{1+\mu_s \cot\theta_r}{1-\mu_s \tan\theta_r} \quad (9)$$

where R is the stress ratio for reactivation and μ_s = 0.39 is our laboratory derived friction coefficient (Figure 11). Following equation 9, the optimum angle for fault reactivation is $\theta_r \approx 34°$ and the corresponding R value is 2.13. This optimum θ_r falls within the range of the most recorded θ_r values (Figure 13). Significant departures from the optimal orientation can be explained through the attainment of local fluid overpressures, as supported by calcite mineralization observed along fault planes.

6.3. Fluid flow controlled by fracture and fault permeability

Within low-permeability lithologies, as in our case study, fracturing and faulting processes are the only mechanisms allowing for fluid flow (e.g., *Odling et al.*, 1999; *Aydin*, 2000; *Agosta and Kirschner*, 2003; *Ferrill et al.*, 2014). The faults observed in the field are characterized by calcite in the form of cement in cataclastic fault rocks, within dilational jogs and in the form of slickenfibers (Figure 6). This field observation suggests that fractures and faults act as conduits during slip events, as further supported by laboratory observations of fracture enhanced permeability (Figure 10). In the field we observe that fractures confined within a single layer (e.g., Figure 5a) do not often show calcite mineralization, whereas faults that cut through the multilayer are marked by calcite mineralization (e.g., Figure 5b). The initiation and reactivation of a fault trajectory that is not planar lead to the development of dilational jogs within the more competent lithology and consequently the opening of void space where fluids can circulate and calcite precipitate (e.g., *Sibson*, 1996). During the initial stages of faulting, fluid circulation can occur within dilational jogs, parallel to the intersection of the fault plane with the bedding, as suggested in previous field studies (e.g., *Sibson*, 1996; *Ferrill and Morris*, 2003). Here, fluid circulation is almost parallel to the bedding and confined within competent layers. However, the presence of calcite mineralization along slip surfaces also in clay-rich layers suggests that, at least during slip, the fault dilates and allows for fluid flow through different layers of the mechanical multilayer. The presence of calcite mineralization within the more mature and foliated fault core indicates that fluid circulation also occurs during fault growth, but the development of a low-permeability foliated fault rock allows for fluid flow only during fluid-assisted fault reactivation.

7. Conclusions

We have investigated the mechanics of fault initiation and evolution within a mechanical multilayer consisting of variously alternated limestones and clay-rich marls, integrating data from outcropping faults and rock deformation experiments on the involved lithologies. Our investigation sheds light on the influence of rock strength and pre-existing anisotropies on fault geometry, fault evolution and fluid assisted fracture permeability.

Fault initiation within the mechanical multilayer is characterized by the development of a staircase trajectory refracting at lithological contrasts. Through limestone layers, the small angles of fault initiation result from the interplay between the strength of intact limestones, responsible for $\theta_i \approx 20° - 30°$, and the reactivation of pre-existing joints at low angle to the maximum principal stress, responsible for $\theta_i \approx 0° - 10°$. Through weak marly layers, most of the angles of fault initiation are higher than predicted by the strength of marls, i.e., 34°, and fault segments often propagate parallel to the foliation in clay-rich layers, suggesting an important role played by the foliation in deflecting fault trajectory. During the incipient stages, marly layers locally develop a dense network of shear fractures, characterized by conjugate planes with dihedral angles of ~90°, suggesting a pressure-independent deformation of these weak layers before fault propagation throughout the multilayer.

With accumulating displacement faults evolve forming straighter trajectories and wider fault cores. At a few meters of displacement, the fault core progressively develops a well-organized marly foliation embedding fragments of limestone. Considering the laboratory-derived friction coefficient of marls, μ_s = 0.39, most of the angles of fault reactivation lay in the field of optimal reactivation, indicating an important role exerted by clay minerals on fault strength.

The presence of different types of calcite mineralization in all the investigated faults (i.e., in cataclastic fault rocks, within dilational jogs and in form of slickenfibers) suggests that faulting is the main mechanism allowing for fluid flow within the sealing layer. Incipient faults promote fluid flow, confined within competent layers, through the opening of dilational jogs. With accumulating displacement, faults develop a low-permeability foliated fault core allowing for fluid flow only during fluid-assisted fault reactivation. This suggests that the sealing integrity of the mechanical multilayer can be affected only by the activity of larger faults cutting across the entire thickness of the sealing layer.

Acknowledgments

This research was carried out within the ERC Starting Grant GLASS (n° 259256). We thank Brett Carpenter and Eugenio Carminati for fruitful discussions and Giovanni Gaglianone for assistance in the laboratory. Reviews by R. Bullock and D. Ferrill significantly helped in improving the manuscript. Our data are available via FTP transfer upon request.

References

Abbate, E., Bortolotti, V., Passerini, P., Sagri, M., 1970. Introduction to the geology of the Northern Apennines. Sedimentary Geology 4(3), 207-249, doi:10.1016/0037-0738(70)90017-5.

Agosta, F., Kirschner, D.L., 2003. Fluid conduits in carbonate-hosted seismogenic normal faults in central Italy. Journal of Geophysical Research: Solid Earth 108(B4), 2221-2234, doi:10.1029/2002JB002013.

Allmendinger, R.W., Cardozo, N.C., Fisher, D., 2012. Structural Geology Algorithms: Vectors and Tensors. Cambridge University Press, Cambridge.

Alvarez, W., 1991. Tectonic evolution of the Corsica-Apennines-Alps region studied by the method of successive approximations. Tectonics, 10, 936-947, doi:10.1029/91TC00232.

Anderson, E.M. 1951. The Dynamics of Faulting and Dyke Formation with Applications to Britain. Oliver & Boyd, Edinburgh.

Antonellini, M., Tondi, E., Agosta, F., Aydin, A., Cello, G., 2008. Failure modes in deep-water carbonates and their impact for fault development: Majella Mountain, Central Apennines, Italy. Marine and Petroleum Geology, 25(10), 1074-1096, doi:10.1016/j.marpetgeo.2007.10.008.

Aydin, A., 2000. Fractures, faults, and hydrocarbon entrapment, migration and flow. Marine and petroleum geology, 17(7), 797-814, doi:10.1016/S0264-8172(00)00020-9.

Bally, A.W., Burbi, L., Cooper, C., Ghelardoni, R., 1986. Balanced sections and seismic reflection profiles across the Central Apennines. Società Geologica Italiana, Memorie 35, 257-310.

Barchi, M.R., Bernasconi, A., Brozzetti, F., Lavecchia, G., Menichetti, M., Minelli, G., Nardon, S, Pialli, G., 1993. Joint distribution in a Fractured Carbonate Reservoir in the Umbria-Marche Anticlines (Central Italy). In: Spencer, A.M. (Ed.), Generation, Accumulation and Production of Europe's Hydrocarbons III, Special Publication of the European Association of Petroleum Geoscientists, Springer, Berlin, 209-217, doi:10.1007/978-3-642-77859-9_17.

Barchi, M.R., Landuzzi, A., Minelli, G., Pialli, G., 2001. Outer northern Apennines. In: Vai, G.B., Martini, I.P. (Eds.), Anatomy of an Orogen: the Apennines and Adjacent Mediterranean Basins, Kluwer Academic Publishers, 215-254, doi: 10.1007/978-94-015-9829-3_15.

Barchi, M.R., Alvarez, W., Shimabukuro, D.H., 2012. The Umbria-Marche Apennines as a double orogen: observations and hypotheses. Italian Journal of Geosciences 131(2), 258-271, doi:10.3301/IJG.2012.17.

Bistacchi, A., Massironi, M., Menegon, L., Bolognesi, F., Donghi, V., 2012. On the nucleation of non-Andersonian faults along phyllosilicate-rich mylonite belts. Geological Society, London, Special Publications, 367(1), 185-199, doi:10.1144/SP367.13.

Bolognesi, F., Bistacchi A., 2016. Weakness and mechanical anisotropy of phyllosilicate-rich cataclasites developed after mylonites of a low-angle normal fault (Simplon Line, Western Alps). Journal of Structural Geology, 83, 1-12, doi:10.1016/j.jsg.2015.11.009.

Bolton, M., 1979. A Guide to Soil Mechanics. John Wiley, New York.

Capuano, N., Levati, E., Merangola, S., Pappafico, G., Pera, M., Tonelli, G., Tosti, S., Tramontana, M., 2009. Carta Geologica d'Italia alla scala 1:50.000, F° 279 Urbino. Servizio Geologico D'Italia.

Carpenter, B.M., Marone, C., Saffer, D.M., 2011. Weakness of the San Andreas Fault revealed by samples from the active fault zone. Nature Geoscience 4, 251-254, doi:10.1038/ngeo1089.

Carmignani, L., Decandia, F. A., Disperati, L., Fantozzi, P. L., Kligfield, R., Lazzarotto, A, Liotta, D., Meccheri, M., 2001. Inner Northern Apennines. In: Vai, G.B., Martini, I.P. (Eds.), Anatomy of an Orogen: the Apennines and Adjacent Mediterranean Basins, Kluwer Academic Publishers, 197-213.

Carminati, E., Doglioni, C., 2012. Alps vs. Apennines: the paradigm of a tectonically asymmetric Earth. Earth-Science Reviews 112(1), 67-96, doi:10.1016/j.earscirev.2012.02.004.

Centamore, E., Jacobacci, A., Malferrari, N., Martelli, G., Pieruccini, U., 1972. Carta Geologica d'Italia alla scala 1:50.000, F° 290 Cagli. Servizio Geologico D'Italia.

Childs, C., Manzocchi, T., Walsh, J. J., Bonson, C. G., Nicol, A., Schöpfer, M. P., 2009. A geometric model of fault zone and fault rock thickness variations. Journal of Structural Geology, 31(2), 117-127, doi:10.1016/j.jsg.2008.08.009.

Crider, J. G., Peacock, D. C. P., 2004. Initiation of brittle faults in the upper crust: a review of field observations. Journal of Structural Geology, 26(4), 691-707, doi:10.1016/j.jsg.2003.07.007.

Coccioni, R., Franchi, R., Nesci, O., Perilli, N., Wezel, F. C., Battistini, F., 1989. Stratigrafia, micropaleontologia e mineralogia delle Marne a Fucoidi (Aptiano inferiore-Albiano superiore) delle sezioni di Poggio le Guaine e del Fiume Bosso (Appennino umbro-marchigiano). Evoluzione, Ambiente, Secondo Convegno Internazionale: Pergola, Italy, Atti, 163-201.

Collettini, C., Viti, C., Smith, S. A. F., Holdsworth, R. E., 2009, Development of interconnected talc networks and weakening of continental low-angle normal faults. Geology, 37(6), 567-570, doi:10.1130/G25645A.1.

Collettini, C., Di Stefano, G., Carpenter, B. M., Scarlato, P., Tesei, T., Mollo, S., Trippetta, F., Marone, C., Romeo, G., Chiaraluce, L., 2014. A novel and versatile apparatus for brittle rock deformation. International Journal of Rock Mechanics and Mining Sciences, 66, 114-123, doi:10.1016/j.ijrmms.2013.12.005.

Corbett, K., Friedman, M., Spang, J., 1987. Fracture development and mechanical stratigraphy of Austin Chalk, Texas. American Association of Petroleum Geologists Bulletin, 71(1), 17-28.

Coulomb, C. A., 1776. Sur une application des règles de maximis et minimis à quèlques problèmes de statique relatifs à l'architecture. Mémoires de Mathématique et de Physique, Académie Royale des Sciences, 7, 343-382.

Doglioni, C., Mongelli, F., Pialli, G., 1998. Appenninic back arc lithospheric boudinage on the former alpine belt. Società Geologica Italiana, Memorie, 52, 457-468.

Donath, F. A., 1961. Experimental study of shear failure in anisotropic rocks. Geological Society of America Bulletin, 72(6), 985-989, doi:10.1130/0016-7606(1961)72[985:ESOSFI]2.0.CO;2.

Engelder, T., 1984. The role of pore water circulation during the deformation of foreland fold and thrust belts. Journal of Geophysical Research: Solid Earth, 89(B6), 4319-4325, doi:10.1029/JB089iB06p04319.

Ferrill, D. A., Morris, A. P., 2003. Dilational normal faults. Journal of Structural Geology, 25(2), 183-196, doi:10.1016/S0191-8141(02)00029-9.

Ferrill, D. A., Morris, A. P., 2008. Fault zone deformation controlled by carbonate mechanical stratigraphy, Balcones fault system, Texas. American Association of Petroleum Geologists Bulletin, 92(3), 359-380, doi:10.1306/10290707066

Ferrill, D. A., Morris, A. P., McGinnis, R. N., Smart, K. J., Ward, W.C., 2011. Fault zone deformation and displacement partitioning in mechanically layered carbonates: The Hidden Valley fault, central Texas. American Association of Petroleum Geologists Bulletin, 95, 1383-1397, doi:10.1306/12031010065.

Ferrill, D. A., McGinnis, R. N., Morris, A. P., Smart, K. J., 2012. Hybrid failure: Field evidence and influence on fault refraction. Journal of Structural Geology, 42, 140-150, doi:10.1016/j.jsg.2012.05.012.

Ferrill, D.A., McGinnis, R.N., Morris, A.P., Smart, K.J., Sickmann, Z.T., Bentz, M., Lehrmann, D., Evans, M.A., 2014. Control of mechanical stratigraphy on bed-restricted jointing and normal faulting: Eagle Ford Formation, south-central Texas, U.S.A. American Association of Petroleum Geologists Bulletin, 98, 2477-2506, doi:10.1306/08191414053.

Giorgioni, M., Tiraboschi, D., Erba, E., Hamann, Y., Weissert, H., 2016. Sedimentary patterns and palaeoceanography of the Albian Marne a Fucoidi Formation (Central Italy) revealed by high-resolution geochemical and nannofossil data. Sedimentology, doi:10.1111/sed.12288.

Gross, M. R., 1995. Fracture partitioning: Failure mode as a function of lithology in the Monterey Formation of coastal California. Geological Society of America Bulletin, 107(7), 779-792, doi:10.1130/0016-7606(1995)107<0779:FPFMAA>2.3.CO;2.

Gross, M. R., Gutie, G., Bai, T., Wacker, M. A., Collinsworth, K. B., Behl, R. J., 1997. Influence of mechanical stratigraphy and kinematics on fault scaling relations. Journal of Structural Geology, 19(2), 171-183, doi:10.1016/S0191-8141(96)00085-5.

Healy, D., 2009. Anisotropy, pore fluid pressure and low angle normal faults. Journal of Structural Geology, 31(6), 561-574, doi:10.1016/j.jsg.2009.03.001.

Hindle, D., Burkhard, M., 1999. Strain, displacement and rotation associated with the formation of curvature in fold belts; the example of the Jura arc. Journal of structural Geology, 21(8), 1089-1101, doi:10.1016/S0191-8141(99)00021-8.

Holdsworth, R.E., 2004. Weak faults – rotten cores. Science 303 (5655), 181 – 182, doi:10.1126/science.1092491.

Jackson, R. E., Dunn, D. E., 1974. Experimental sliding friction and cataclasis of foliated rocks. International Journal of Rock Mechanics and Mining Sciences, 11(6), 235-249, doi:10.1016/0148-9062(74)90130-2

Jaeger, J. C., 1960. Shear failure of anistropic rocks. Geological Magazine, 97(01), 65-72, doi:10.1130/0016-7606(1961)72[985:ESOSFI]2.0.CO;2.

Jaeger, J. C., Cook, N. G. W, 1979. Fundamentals of rock mechanics. Chapman & Haii, London.

Koopman, A., 1983. Detachment tectonics in the Central Apennines, Italy. Geologica Ultraiectina, 30, 155.

Kristensen, M. B., Childs, C., Olesen, N. Ø., Korstgård, J. A., 2013. The microstructure and internal architecture of shear bands in sand–clay sequences. Journal of Structural Geology, 46, 129-141, doi:10.1016/j.jsg.2012.09.015.

Lavecchia, G., Minelli, G., Pialli, G., 1988. The Umbria-Marche arcuate fold belt (Italy). Tectonophysics, 146(1), 125-137, doi:10.1016/0040-1951(88)90086-8.

Li, J., Hu, X., Zhao, K., Cai, Y., Sun, T., 2016. Paleoceanographic evolution and chronostratigraphy of the Aptian Oceanic Anoxic Event 1a (OAE1a) to oceanic red bed 1 (ORB1) in the Gorgo a Cerbara section (central Italy). Cretaceous Research, 66, 115-128, doi:10.1016/j.cretres.2016.04.016.

Mandl, G. G., 1988. Mechanics of tectonic faulting: models and basic concepts. Elsevier, New York.

Manzocchi, T., Heath, A. E., Palananthakumar, B., Childs, C., Walsh, J. J., 2008. Faults in conventional flow simulation models: a consideration of representational assumptions and geological uncertainties. Petroleum Geoscience, 14, 91–110, doi:10.1144/1354-079306-775.

Manzocchi, T., Childs, C., Walsh, J. J., 2010. Faults and fault properties in hydrocarbon flow models. Geofluids, 10(1-2), 94-113, doi:10.1111/j.1468-8123.2010.00283.x.

Marinos, P., Hoek, E., 2001. Estimating the geotechnical properties of heterogeneous rock masses such as flysch. Bulletin of the Engineering Geology & the Environment, 60, 85-92, doi:10.1007/s100640000090.

Marrett, R., Allmendinger, R. W., 1990. Kinematic analysis of fault-slip data. Journal of Structural Geology, 12(8), 973-986, doi:10.1016/0191-8141(90)90093-E.

Marshak, S., Geiser, P. A., Alvarez, W., Engelder, T., 1982. Mesoscopic fault array of the northern Umbrian Apennine fold belt, Italy: Geometry of conjugate shear by pressure-solution slip. Geological Society of America Bulletin, 93(10), 1013-1022, doi:10.1130/0016-7606(1982)93<1013:MFAOTN>2.0.CO;2.

Massironi, M., Bistacchi, A., Menegon, L., 2011. Misoriented faults in exhumed metamorphic complexes: Rule or exception? Earth and Planetary Science Letters, 307, 233-239, doi:10.1016/j.epsl.2011.04.041.

McCabe, W., Koerner R. M., 1975. High pressure shear strength investigation of an anisotropic mica schist rock. International Journal of Rock Mechanics and Mining Sciences, 12(8), 219-228, doi:10.1016/0148-9062(75)91402-3.

Misra, S., Ellis, S., Mandal, N., 2015. Fault damage zones in mechanically layered rocks: The effects of planar anisotropy. Journal of Geophysical Research: Solid Earth, 120(8), 5432-5452, doi:10.1002/2014JB011780.

Nicol, A., Watterson, J., Walsh, J. J., Childs, C., 1996. The shapes, major axis orientations and displacement patterns of fault surfaces. Journal of Structural Geology, 18(2), 235-248, doi:10.1016/S0191-8141(96)80047-2.

Odling, N.E., Gillespie, P., Bourgine, B., Castaing, C., Chilés, J.-P., Christensen, N.P., Fillion, E., Genter, A., Olsen, C., Thrane, L., Trice, R., Aarseth, E., Walsh, J.J., Watterson, J., 1999. Variations in fracture system geometry and their implications for fluid flow in fractured hydrocarbon reservoirs. Petroleum Geoscience, 5, 373-384, doi:10.1144/petgeo.5.4.373.

Paterson, M. S., Wong, T.-F., 2005. Experimental rock deformation-the brittle field, 2nd ed., Springer, New York.

Peacock, D. C. P., Sanderson, D. J., 1992. Effects of layering and anisotropy on fault geometry. Journal of the Geological Society, 149(5), 793-802, doi:10.1144/gsjgs.149.5.0793.

Price, N.J., Cosgrove, J.W., 1990. Analysis of Geological Structures. Cambridge University Press, Cambridge.

Ramsay, J. G., Huber, M. I., 1987. The techniques of modern structural geology: Folds and fractures (Vol. 2). Academic Press., San Diego.

Ramsey, J.M., Chester, F.M., 2004. Hybrid fracture and the transition from extension fracture to shear fracture. Nature 428, 63-66, doi:10.1038/nature02333.

Reutter, K.-J., Giese, P., Closs, H., 1980. Lithospheric split in the descending plate: observations from the Northern Apennines. Tectonophysics 64, 1-9. doi:10.1016/0040-1951(80) 90254-1.

Rice, J. R., 1975. On the stability of dilatant hardening for saturated rock masses. Journal of Geophysical Research, 80(11), 1531-1536, doi:10.1029/JB080i011p01531.

Roche, V., Homberg, C., Rocher, M., 2012. Architecture and growth of normal fault zones in multilayer systems: A 3D field analysis in the South-Eastern Basin, France. Journal of Structural Geology, 37, 19-35, doi:10.1016/j.jsg.2012.02.005.

Rudnicki, J. W., Rice, J. R., 1975. Conditions for the localization of deformation in pressure-sensitive dilatant materials. Journal of the Mechanics and Physics of Solids, 23(6), 371-394, doi:10.1016/0022-5096(75)90001-0.

Rudnicki, J. W., 1984. Effects of dilatant hardening on the development of concentrated shear deformation in fissured rock masses. Journal of Geophysical Research: Solid Earth, 89(B11), 9259-9270, doi:10.1029/JB089iB11p09259.

Rudnicki, J.W., 2002. Diffusive instabilities in dilating and compacting geomaterials. In: Chuang, T.-J., Rudnicki, J.W. (Eds.), Multiscale Deformation and Fracture in Materials and Structures. Kluwer Academic Publishers, Dordrecht, doi:10.1007/0-306-46952-9_10.

Runesson, K., Perić, D., Sture, S., 1996. Effect of pore fluid compressibility on localization in elastic-plastic porous solids under undrained conditions. International Journal of Solids and Structures, 33(10), 1501-1518, doi:10.1016/0020-7683(95)00104-2.

Schofield, A. N., Wroth, P., 1968. Critical State Soil Mechanics. McGraw-Hill, New York.

Schöpfer, M. P., Childs, C., Walsh, J. J., 2006. Localisation of normal faults in multilayer sequences. Journal of Structural Geology, 28(5), 816-833, doi:10.1016/j.jsg.2006.02.003.

Schöpfer, M. P., Childs, C., Walsh, J. J., Manzocchi, T., Koyi, H. A., 2007. Geometrical analysis of the refraction and segmentation of normal faults in periodically layered sequences. Journal of Structural Geology, 29(2), 318-335, doi:10.1016/j.jsg.2006.08.006.

Scuderi, M.M., Collettini, C., 2016. The role of fluid pressure in induced vs. triggered seismicity: insights from rock deformation experiments on carbonates. Scientific Reports, 6, 24852, doi:10.1038/srep24852.

Shea, W. T., Kronenberg, A. K., 1993. Strength and anisotropy of foliated rocks with varied mica contents. Journal of Structural Geology, 15(9), 1097-1121, doi:10.1016/0191-8141(93)90158-7.

Sibson, R. H., 1985. A note on fault reactivation. Journal of Structural Geology, 7(6), 751-754, doi:10.1016/0191-8141(85)90150-6.

Sibson, R. H., 1996. Structural permeability of fluid-driven fault-fracture meshes. Journal of Structural Geology, 18(8), 1031-1042, doi:10.1016/0191-8141(96)00032-6.

Sylvester, A. G., 1988. Strike-slip faults. Geological Society of America Bulletin, 100(11), 1666-1703, doi:10.1130/0016-7606(1988)100<1666:SSF>2.3.CO;2.

Soliva, R., Benedicto, A., 2005. Geometry, scaling relations and spacing of vertically restricted normal faults. Journal of Structural Geology, 27(2), 317-325, doi:10.1016/j.jsg.2004.08.010.

Tesei, T., Collettini, C., Barchi, M. R., Carpenter, B. M., Di Stefano G., 2014. Heterogeneous strength and fault zone complexity of carbonate-bearing thrusts with possible implications for seismicity. Earth and Planetary Science Letters, 408, 307-318, doi:10.1016/j.epsl.2014.10.021.

Tesei, T., Lacroix, B., Collettini, C., 2015. Fault strength in thin-skinned tectonic wedges across the smectite-illite transition: Constraints from friction experiments and critical tapers. Geology, 43(10), 923-926, doi:10.1130/G36978.1.

Tembe, S., Lockner, D. A., Wong, T. -F., 2010. Effect of clay content and mineralogy on frictional sliding behavior of simulated gouges: Binary and ternary mixtures of quartz, illite, and montmorillonite. Journal of Geophysical Research, 115, B03416, doi:10.1029/2009JB006383.

Tornaghi, M.E., Premoli, Silva I., Ripepe, M.,1989. Lithostratigraphy and planktonic foraminiferal biostratigraphy of the aptian-albian “Scisti a Fucoidi” in the Piobbico core, Marche, Italy: background for cyclostratigraphy. Rivista Italiana di Paleontologia e Stratigrafia, 95(3), 223-264.

Wilkins, S. J., Gross, M. R., Wacker, M., Eyal, Y., Engelder, T., 2001. Faulted joints: kinematics, displacement–length scaling relations and criteria for their identification. Journal of Structural Geology, 23(2), 315-327, doi:10.1016/S0191-8141(00)00098-5.

Wilkins, S. J., Gross, M. R., 2002. Normal fault growth in layered rocks at Split Mountain, Utah: influence of mechanical stratigraphy on dip linkage, fault restriction and fault scaling. Journal of Structural Geology, 24(9), 1413-1429, doi:10.1016/S0191-8141(01)00154-7

Wong, T. F., David, C., Zhu, W., 1997. The transition from brittle faulting to cataclastic flow in porous sandstones: Mechanical deformation. Journal of Geophysical Research: Solid Earth, 102(B2), 3009-3025, doi:10.1029/96JB03281.

Table

Experiment number	Material	$CaCO_3$ content[a] (wt.%)	Configuration	Applied stresses (MPa)	Deformation velocity[b] (μm/s)
i424	marly limestone	83	triaxial	$P_c = 10$	$V_a = 0.1$
i426	marly limestone	83	triaxial	$P_c = 20$	$V_a = 0.1$
i431	marly limestone	83	triaxial	$P_c = 30$	$V_a = 0.1$
i432	marly limestone with chert	72	triaxial	$P_c = 10$	$V_a = 0.1$
i435	marly limestone with chert	72	triaxial	$P_c = 20$	$V_a = 0.1$
i436	marly limestone with chert	72	triaxial	$P_c = 30$	$V_a = 0.1$
i469	marls	59	biaxial	$P_c = 15$ $\sigma_n = 20$	$V_s = 10$
i485	marls	59	biaxial	$P_c = 15$ $\sigma_n = 30$ - 40 -50	$V_s = 10$

[a] $CaCO_3$ content determined using a Dietrich-Fruhling calcimeter.
[b] axial velocity (v_a) in triaxial experiments and sliding velocity (v_s) in biaxial experiments.

Table 1. Details of the experiments performed.

Figures Captions

Figure 1. (a) Digital elevation model of the Northern Umbria-Marche Apennines created using GeoMapApp (http://www.geomapapp.org) displaying traces of main thrusts and normal faults. (b) Geological map of Mt. Montiego anticline area (after *Centamore et al.*, 1972; *Capuano et al.*, 2009), showing the location of the studied outcrops. (c) Stratigraphic succession in the study area.

Figure 2. (a) The BRAVA rock deformation apparatus (after *Scuderi and Collettini*, 2016): two load cells, measuring vertical (F_v) and horizontal forces (F_h), are located within the pressure vessel designed to support the vertical and the horizontal pistons. Two high-pressure ports allow the communication between the sample assembly and the up- and down-stream pressure intensifiers. One high-pressure access port allows the communication between the pressure vessel and the confining oil intensifier. (b) Triaxial configuration within the pressure vessel. Confining oil is used to apply an isotropic pressure ($\sigma_3 = \sigma_2$) and the vertical loading frame applies a vertical force generating a differential stress. Pore pressure lines show the direction of the fluid flow during the experiment. (c) Double direct shear configuration within the pressure vessel and (d) a schematic representation of the configuration contained within the jacket (orange in figure c). In this configuration three stainless steel forcing blocks sandwich two identical layers of experimental fault gouge. The sample assembly consists of forcing blocks, equipped with internal channels for pore fluids, porous frits and rubber jacket (latex tubes and boots).

Figure 3. (a) Fault system in the marl-rich multilayer (outcrop A, 302690 N 4830479 E UTM coordinates 33T zone). Fault trajectories are complex especially for small displacements. Right-lateral faults, accumulating 1-10 cm of displacement, show undulate trajectories with segments propagating parallel to the layering in clay-rich layers (yellow arrows). The main left-lateral fault (dashed red line), showing 1-2 m of displacement, has an overall straight trajectory refracting at the

boundary between the reddish and the greyish brown marly portion. Inset shows the orientation of the local stress field derived from the orientation of extensional fractures and conjugate faults. (b) Incipient fault displaying a staircase trajectory that results in dilational jogs within more competent limestone layers. (c) Fault with about 10 cm displacement displaying an almost straight trajectory in its lower portion; in the uppermost part of the fault, within clay-rich layers, the displacement is partitioned into different splays. (d) The main left-lateral fault in (a) does not refract at competence contrast between single layers and shows an approximately 10 cm wide fault core, characterized by duplexes of competent limestone surrounded by a foliated marly matrix.

Figure 4. (a) Fault system in the limestone-rich multilayer (outcrop B, 302684 N 4830502 E UTM coordinates 33T zone). Fault trajectories are complex especially for small displacements. Faults with ~10 cm of displacement develop segments propagating parallel to the layering in clay-rich layers (yellow arrows). Inset shows the orientation of the local stress field derived from the orientation of extensional fractures and conjugate faults. (b) Fault with a few centimeters of displacement showing refraction at competence contrast with high θ_i values in clay-rich layers and small θ_i values in limestone layers. (c) Fault with displacement of a few decimeters showing a straight trajectory that results from the cutting and reworking of a dilational jog, developing an intensely fractured region (blue arrows). (d) Fault with metric displacement displaying a wide fault core with limestone fragments embedded in clay-rich matrix.

Figure 5. Fault initiation in the mechanical multilayer. (a) Local increase of fracturing within marly layers, showing dihedral angles of ~90° between conjugate fracture planes. (b) Fractures propagating throughout the multilayer. All the fractures are filled with calcite mineralization (light blue arrows).

Figure 6. Types of calcite mineralization along faults. (a) Dilational jogs filled with blocky calcite. (b) Dilational jog filled with calcite having a growth direction (blue arrows) oblique to the wall of the fracture. (c) Slickenfibers of calcite along a fault cutting a competent layer. (d) Slickenfibers along faults developing in clay-rich layers. (e) Cataclastic fault rock developed from a competent layer, deeply reworked and cemented in a calcite matrix.

Figure 7. Fault with a large (20 m) displacement (Outcrop C, 302628 N 4830455 E UTM coordinates 33T zone), putting into contact a marl-rich group of layers (unit A, above) with a limestone-rich group of layers (unit B, below). (a) The mature fault develops a well-organized, foliated fault core, characterized by an SCC' fabric. The fault surface shows an overall straight trajectory, but its boundaries still maintain the original staircase shape, resulting in a variable thickness of the fault core, ranging from 5 cm to 45 cm. Inset shows the orientation of faults, extensional fractures and bedding. (b) Detail of the fault zone, mostly consisting of reddish marl from the marly unit A, where the SCC' fabric is evident; note the thin ultracataclasite layer at the lower boundary of the fault core, which is derived from the limestone-rich unit B. (c) The lower boundary of the fault core preserves well the initial staircase geometry.

Figure 8. (a) Local stress fields determined using conjugate fault planes at outcrop A (right, Figure 3a) and B (left, Figure. 4a). Overall stress field: slickenfibers and striae orientation with kinematic tensors calculated using a linked Bingham distribution method (Marrett and Allmendiger, 1990; Allmendiger et al., 2012). The three diagrams show a consistent orientation of the stress field, with a nearly N-S trending maximum principal stress axis. (b) Frequency histograms showing the distribution of θ_i and θ_r angles. θ_i values are small in competent limestone layers, ranging from 5° to 28°, and large in incompetent marly layers, ranging from 32° to 86°. θ_r values show a bell-shaped distribution with values ranging between θ_r = 17° and θ_r = 72°.

Figure 9. Results from triaxial loading experiments on marly limestones. (a) Evolution of differential stress with increasing axial strain for the tested samples (limestone and limestone with chert) at different confining pressures (P_c = 10-30 MPa). All the experiments show a stress drop after the attainment of a peak value of differential stress. With increasing confining pressure the stress drop is smaller and less sharp. (b) Differential stress at peak strength plotted against the mean stress. Linear regression of peak strength values, excluding the samples where nodules of chert are cut by fractures (10 and 20 MPa), shows M = 1.54 and C = 66.18 (Equation 7).

Figure 10. Fracture-enhanced permeability during triaxial experiments at 10 MPa confining pressure. (a) Pore fluid volume remains constant during loading and strongly increases immediately after the stress drop. (b) Failed sample displaying a through-going fracture from the bottom to the top of the rock cylinder, thus explaining the strong increase in pore fluid volume.

Figure 11. Results from biaxial loading experiments on marls. (a) Shear stress evolution with increasing shear strain. During the experiment, shear stress increases until the attainment of a peak value τ_p and then evolves to a steady-state value τ_{ss}. (b) Shear stress at peak and steady-state plotted against normal stress. The envelope of peak shear stresses results in friction μ_i = 0.42, whereas the envelope of steady-state stresses results in lower friction μ_s = 0.39.

Figure 12. Fault initiation in limestones. We consider the Coulomb failure envelope derived from laboratory experiments for intact limestones and an envelope with the same friction but without cohesion for the reactivation of pre-existing surfaces within limestone. (a) Stress state able to explain the simultaneous initiation of shear fractures and reactivation of joints (discontinuities). In competent layers, when σ_1 and σ_3 are both positive, the initiation of faults with θ_i of ~26° and the reactivation of pre-existing surfaces with θ_r between 3° and 48° can simultaneously occur (cf. also the inset, showing the range of unstable orientations for pre-existing fractures, i.e., $2\theta_r$ = 7 - 96°). In

the studied outcrops most of the pre-existing surfaces in calcite-rich layers are joints at low angles, 0 - 20° in Figure 8b, to σ_1. (b) Stress state able to explain the simultaneous initiation of hybrid fractures and reactivation of joints and foliation. In competent layers, when σ_3 is negative, and therefore under small differential stress and high fluid pressure conditions, the initiation of hybrid fractures with θ_i of ~20° and the reactivation of pre-existing surfaces with θ_r between 0° and 58° can simultaneously occur.

Figure 13. Stress ratio, $R = \sigma_1/\sigma_3$, for frictional reactivation of a cohesionless fault (e.g., *Sibson*, 1985) plotted against the reactivation angle, θ_r, for a friction value of $\mu_s = 0.39$, that is the value obtained from biaxial experiments (see Figure 11b). The distribution of reactivation angles, θ_r, measured for outcropping faults is consistent with a friction value of $\mu_s = 0.39$.

Figures

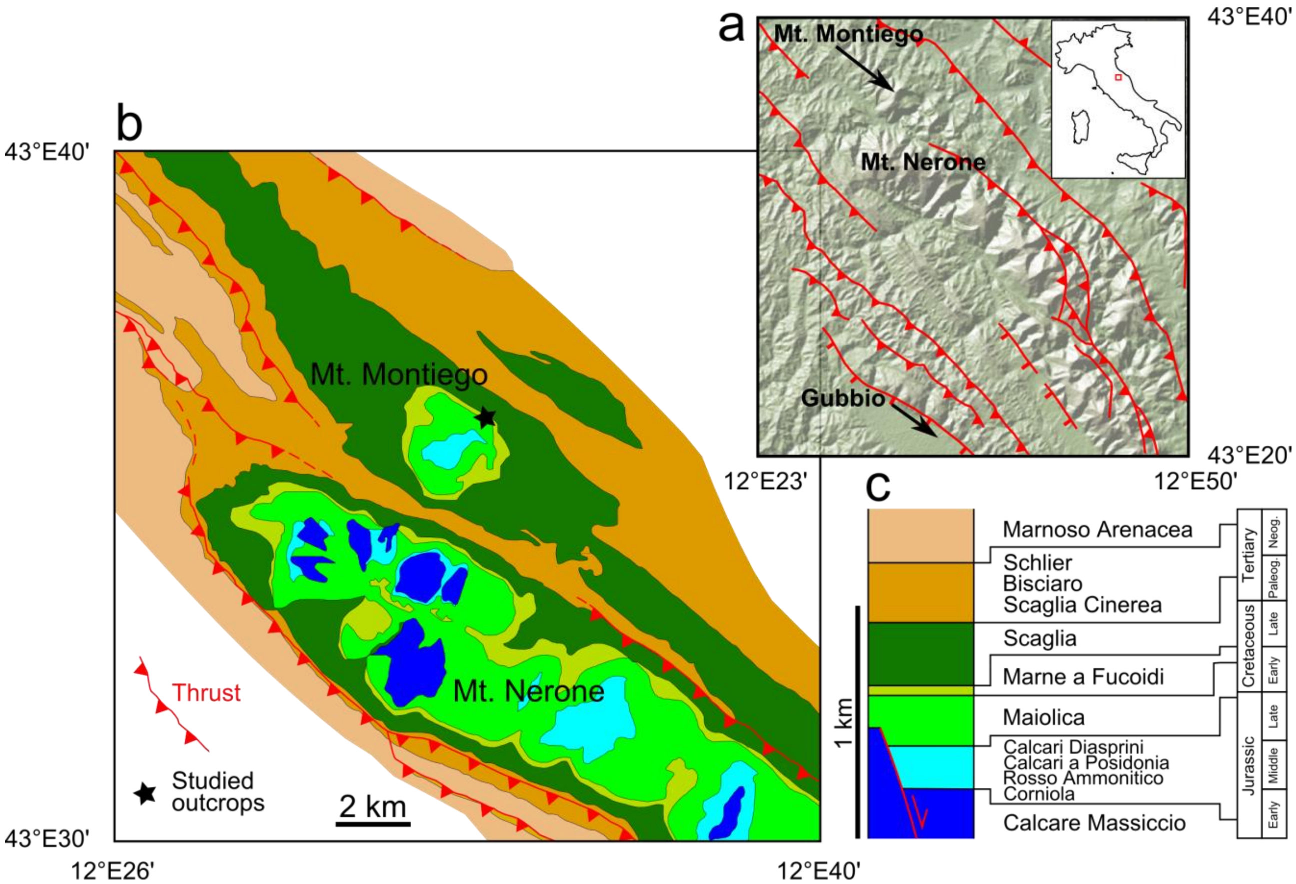

Figure 1. (a) Digital elevation model of the Northern Umbria-Marche Apennines created using GeoMapApp (http://www.geomapapp.org) displaying traces of main thrusts and normal faults. (b) Geological map of Mt. Montiego anticline area (after *Centamore et al.*, 1972; *Capuano et al.*, 2009), showing the location of the studied outcrops. (c) Stratigraphic succession in the study area.

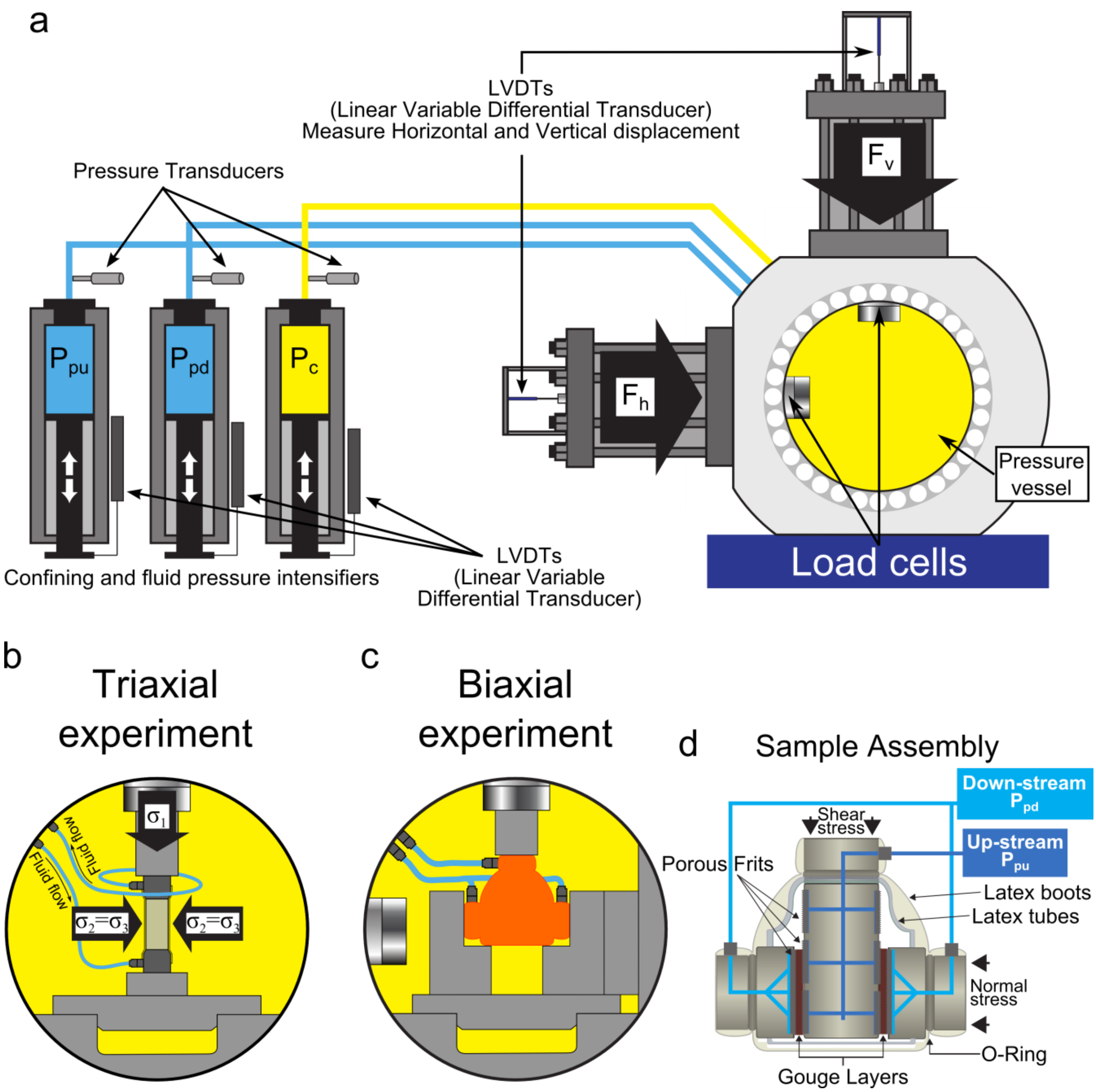

Figure 2. (a) The BRAVA rock deformation apparatus (after *Scuderi and Collettini*, 2016): two load cells, measuring vertical (F_v) and horizontal forces (F_h), are located within the pressure vessel designed to support the vertical and the horizontal pistons. Two high-pressure ports allow the communication between the sample assembly and the up- and down-stream pressure intensifiers. One high-pressure access port allows the communication between the pressure vessel and the confining oil intensifier. (b) Triaxial configuration within the pressure vessel. Confining oil is used to apply an isotropic pressure (σ_3 = σ_2) and the vertical loading frame applies a vertical force generating a differential stress. Pore pressure lines show the direction of the fluid flow during the

experiment. (c) Double direct shear configuration within the pressure vessel and (d) a schematic representation of the configuration contained within the jacket (orange in figure c). In this configuration three stainless steel forcing blocks sandwich two identical layers of experimental fault gouge. The sample assembly consists of forcing blocks, equipped with internal channels for pore fluids, porous frits and rubber jacket (latex tubes and boots).

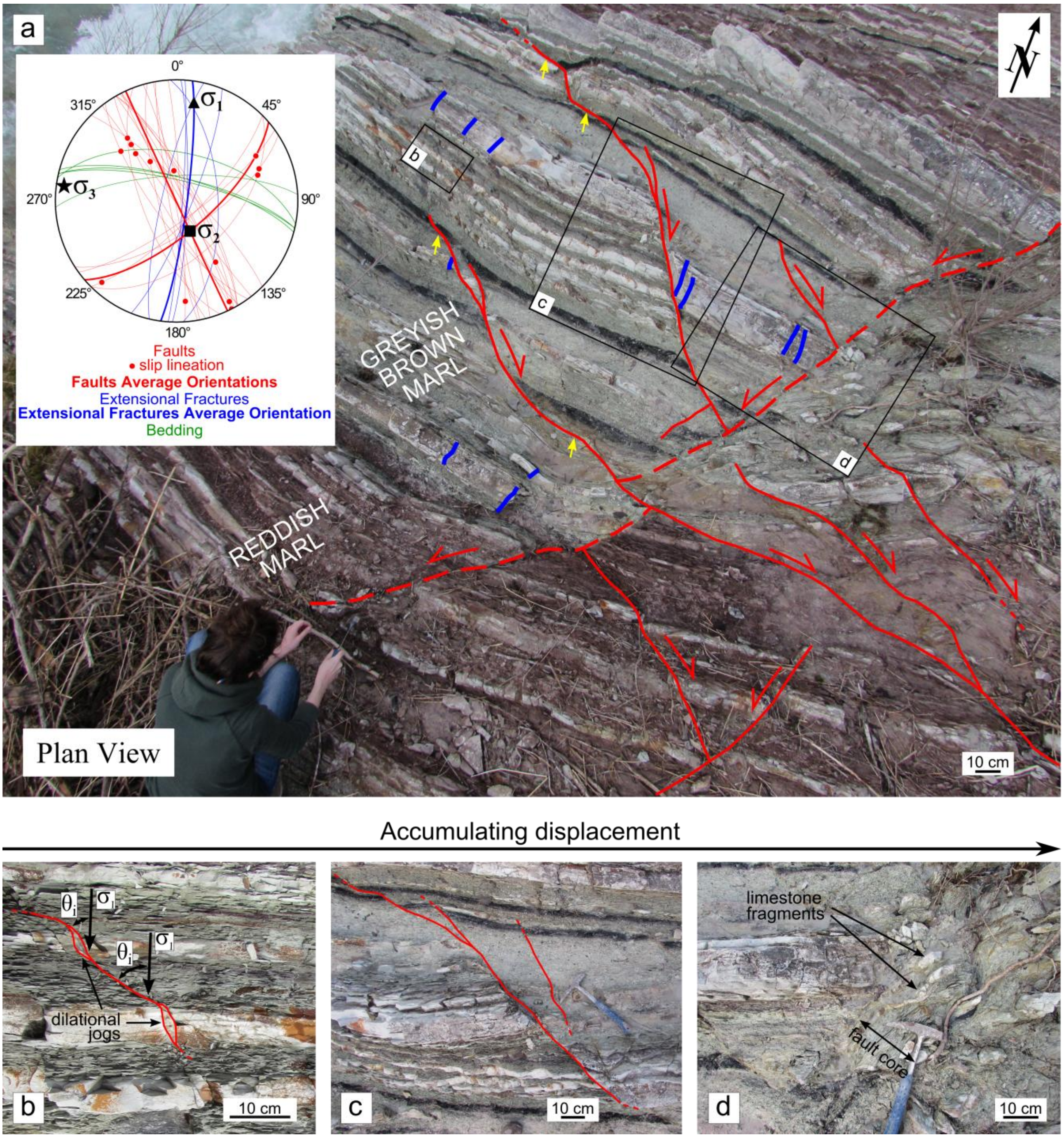

Figure 3. (a) Fault system in the marl-rich multilayer (outcrop A, 302690 N 4830479 E UTM coordinates 33T zone). Fault trajectories are complex especially for small displacements. Right-lateral faults, accumulating 1-10 cm of displacement show undulate trajectories with segments propagating parallel to the layering in clay-rich layers (yellow arrows). The main left-lateral fault (dashed red line), showing 1-2 m of displacement, has an overall straight trajectory refracting at the boundary between the reddish and the greyish brown marly portion. Inset shows the orientation of the local stress field derived from the orientation of extensional fractures and conjugate faults. (b)

Incipient fault displaying a staircase trajectory that results in dilational jogs within more competent limestone layers. (c) Fault with about 10 cm displacement displaying an almost straight trajectory in its lower portion; in the uppermost part of the fault, within clay-rich layers, the displacement is partitioned into different splays. (d) The main left-lateral fault in (a) does not refract at competence contrast between single layers and shows an approximately 10 cm wide fault core, characterized by duplexes of competent limestone surrounded by a foliated marly matrix.

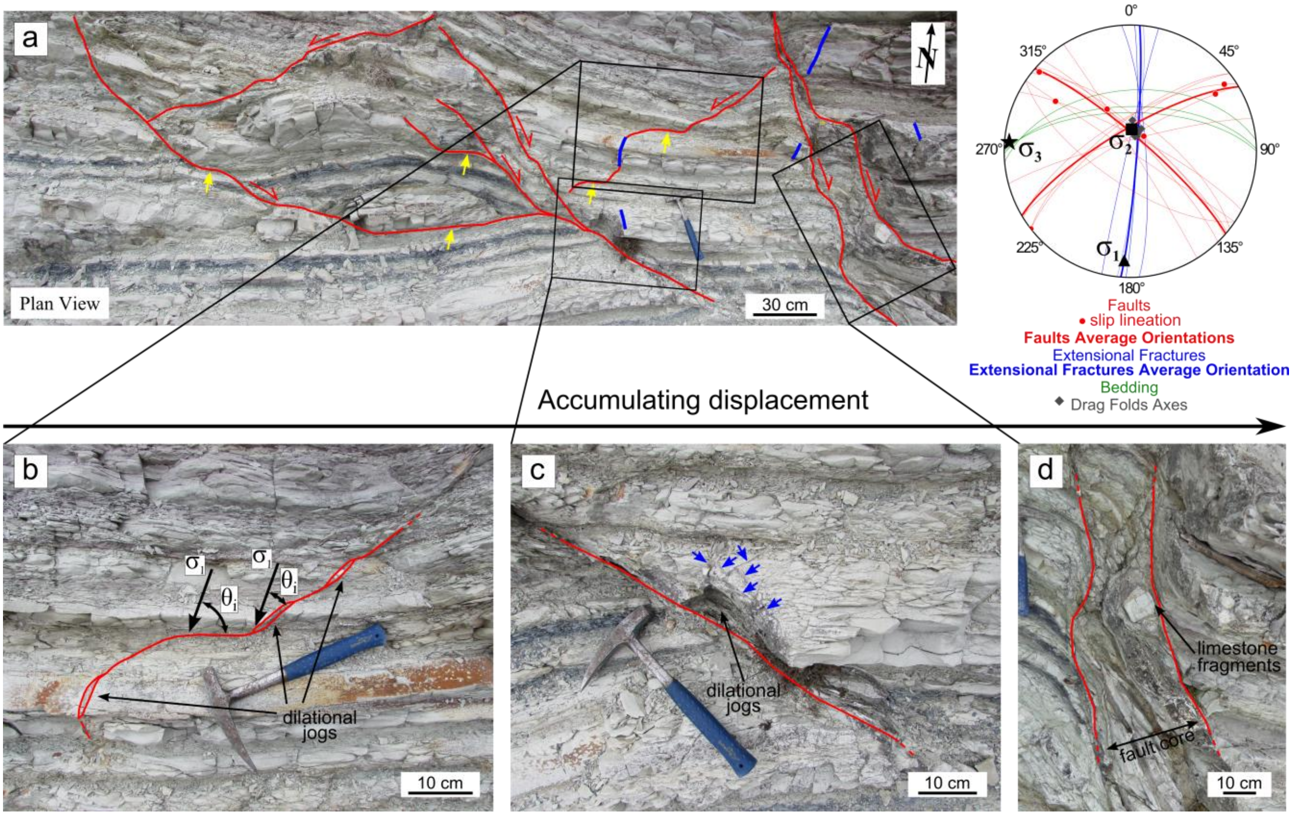

Figure 4. (a) Fault system in the limestone-rich multilayer (outcrop B, 302684 N 4830502 E UTM coordinates 33T zone). Fault trajectories are complex especially for small displacements. Faults with ~10 cm of displacement develop segments propagating parallel to the layering in clay-rich layers (yellow arrows). Inset shows the orientation of the local stress field derived from the orientation of extensional fractures and conjugate faults. (b) Fault with a few centimeters of displacement showing refraction at competence contrast with high θ_i values in clay-rich layers and small θ_i values in limestone layers. (c) Fault with displacement of a few decimeters showing a straight trajectory that results from the cutting and reworking of a dilational jog, developing an intensely fractured region (blue arrows). (d) Fault with metric displacement displaying a wide fault core with limestone fragments embedded in clay-rich matrix.

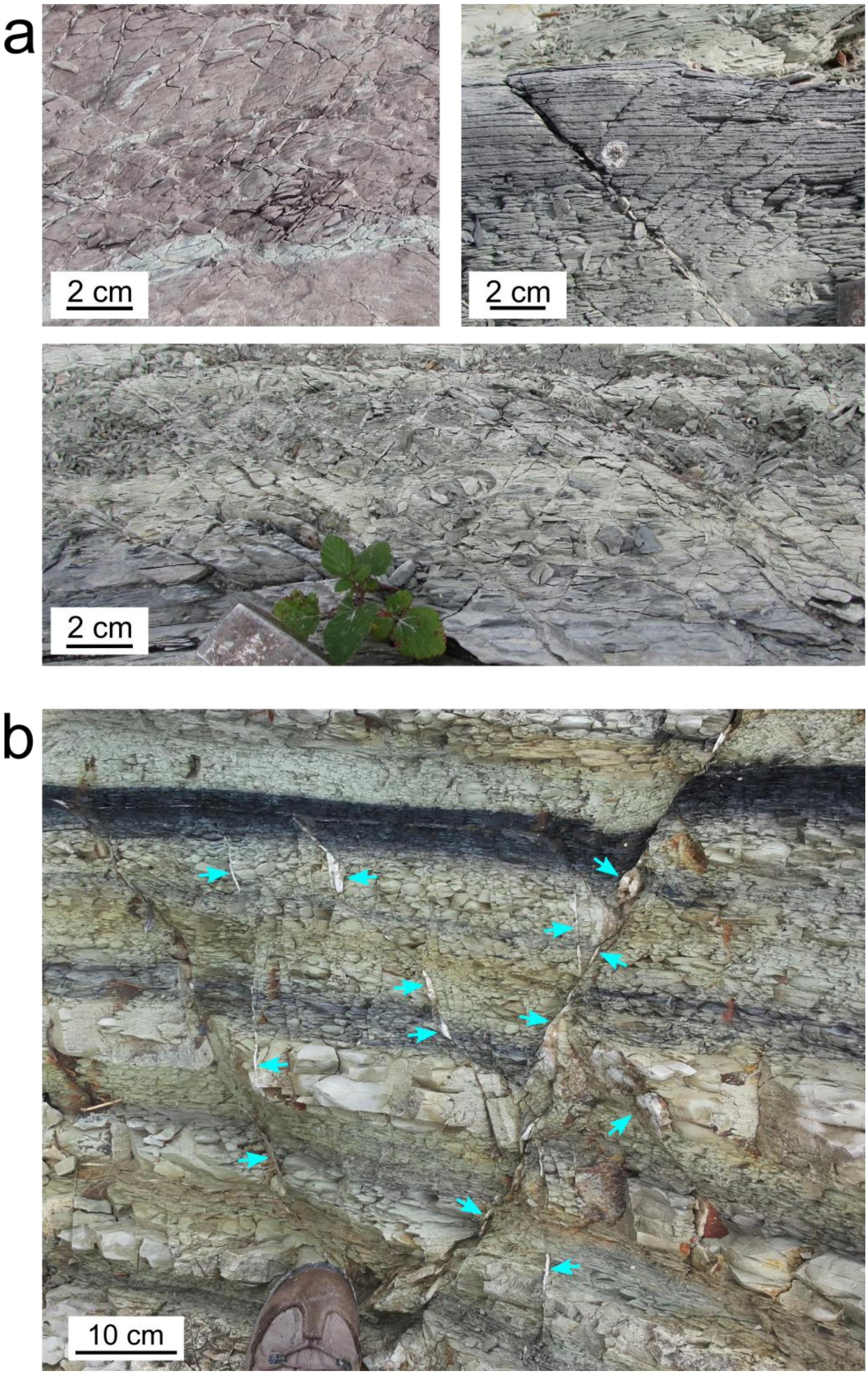

Figure 5. Fault initiation in the mechanical multilayer. (a) Local increase of fracturing within marly layers, showing dihedral angles of ~90° between conjugate fracture planes. (b) Fractures propagating throughout the multilayer. All the fractures are filled with calcite mineralization (light blue arrows).

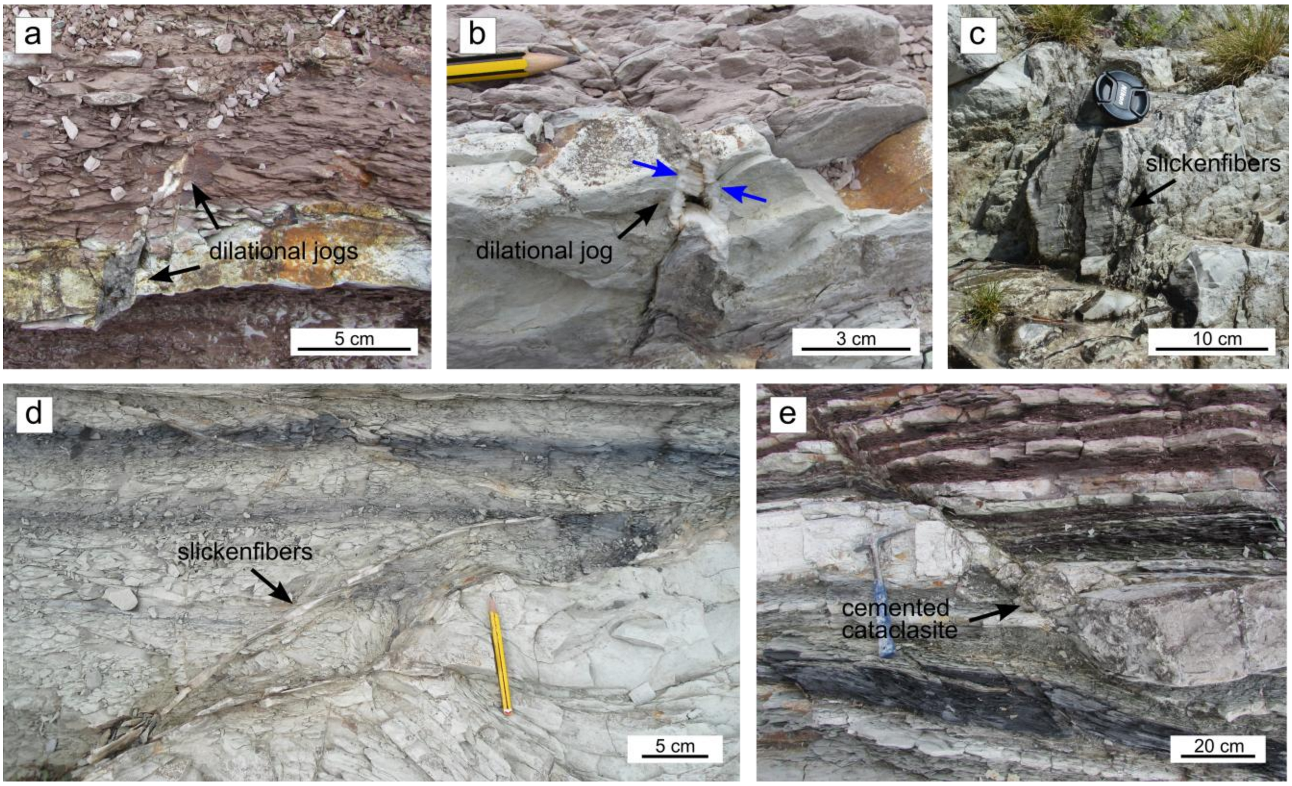

Figure 6. Types of calcite mineralization along faults. (a) Dilational jogs filled with blocky calcite. (b) Dilational jog filled with calcite having a growth direction (blue arrows) oblique to the wall of the fracture. (c) Slickenfibers of calcite along a fault cutting a competent layer. (d) Slickenfibers along faults developing in clay-rich layers. (e) Cataclastic fault rock developed from a competent layer, deeply reworked and cemented in a calcite matrix.

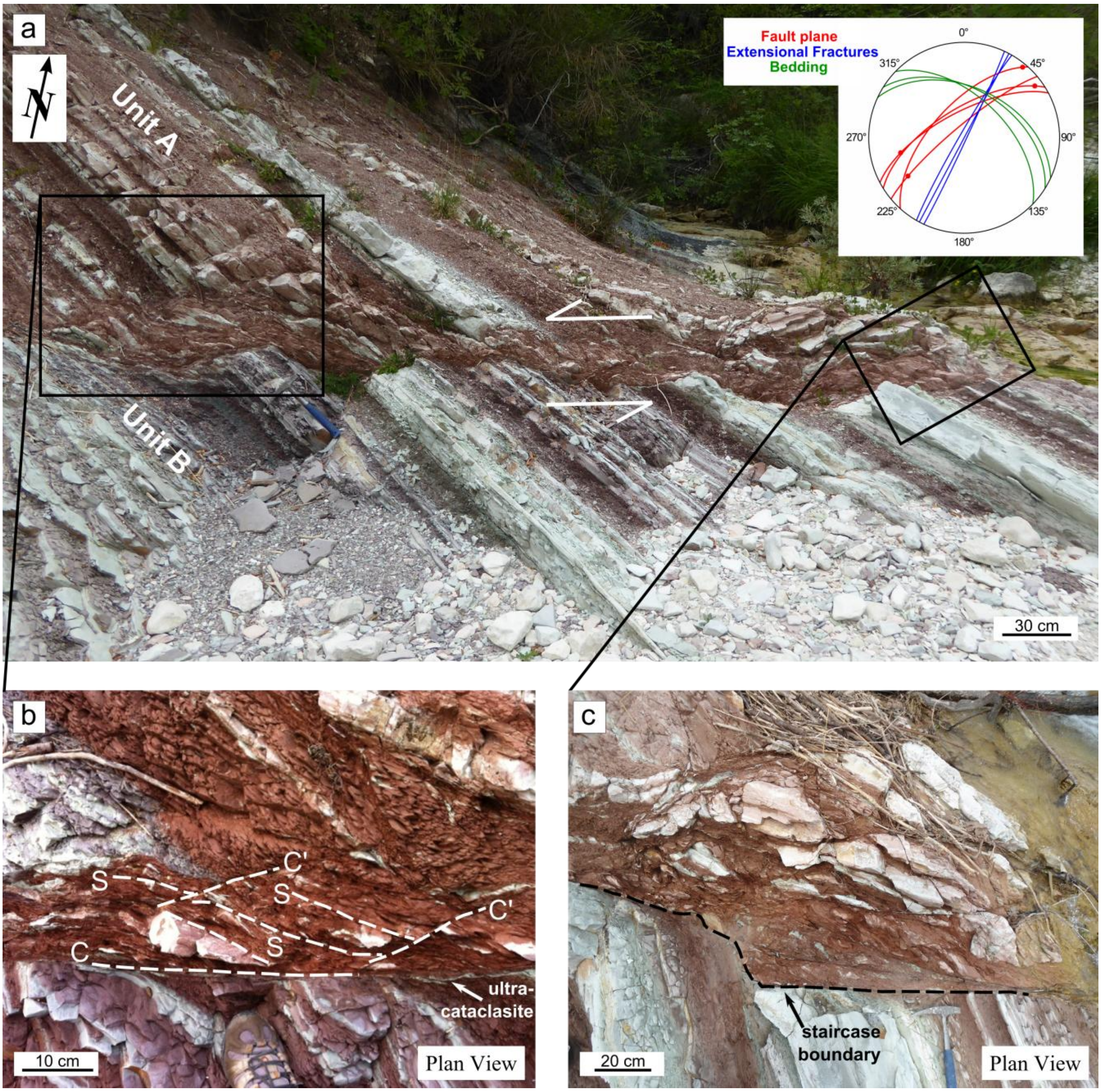

Figure 7. Fault with a large (20 m) displacement (Outcrop C, 302628 N 4830455 E UTM coordinates 33T zone), putting into contact a marl-rich group of layers (unit A, above) with a limestone-rich group of layers (unit B, below). (a) The mature fault develops a well-organized, foliated fault core, characterized by an SCC' fabric. The fault surface shows an overall straight trajectory, but its boundaries still maintain the original staircase shape, resulting in a variable thickness of the fault core, ranging from 5 cm to 45 cm. Inset shows the orientation of faults, extensional fractures and bedding. (b) Detail of the fault zone, mostly consisting of reddish marl from the marly unit A, where the SCC' fabric is evident; note the thin ultracataclasite layer at the

lower boundary of the fault core, which is derived from the limestone-rich unit B. (c) The lower boundary of the fault core preserves well the initial staircase geometry.

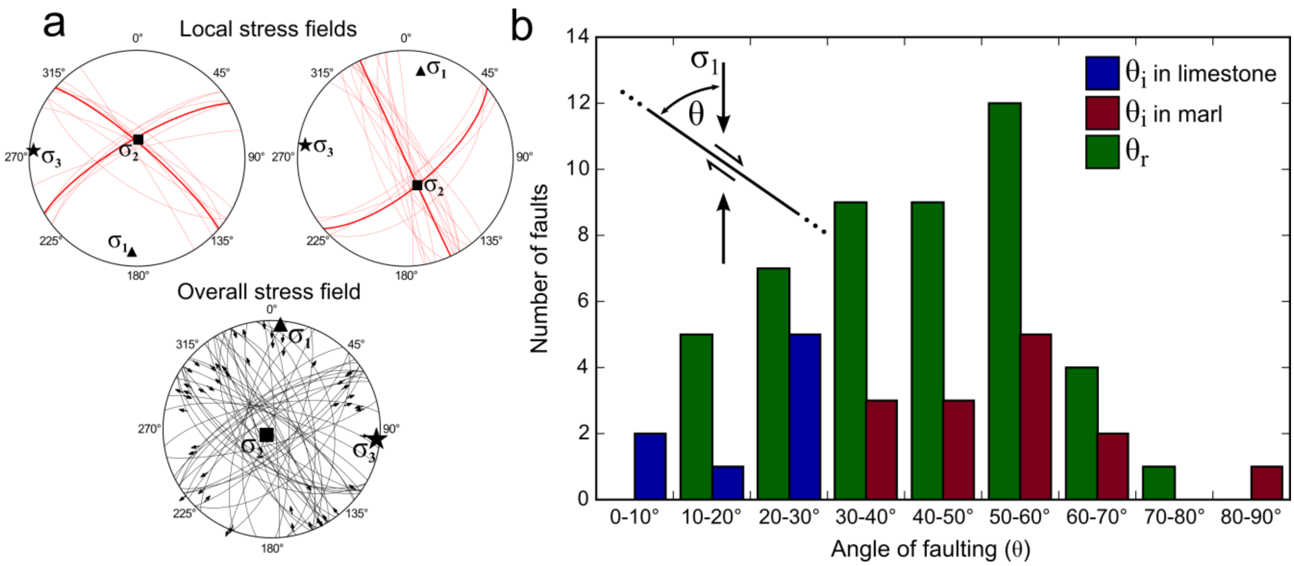

Figure 8. (a) Local stress fields determined using conjugate fault planes at outcrop A (right, Figure 3a) and B (left, Figure. 4a). Overall stress field: slickenfibers and striae orientation with kinematic tensors calculated using a linked Bingham distribution method (*Marrett and Allmendiger*, 1990; *Allmendiger et al.*, 2012). The three diagrams show a consistent orientation of the stress field, with a nearly N-S trending maximum principal stress axis. (b) Frequency histograms showing the distribution of θ_i and θ_r angles. θ_i values are small in competent limestone layers, ranging from 5° to 28°, and large in incompetent marly layers, ranging from 32° to 86°. θ_r values show a bell-shaped distribution with values ranging between θ_r = 17° and θ_r = 72°.

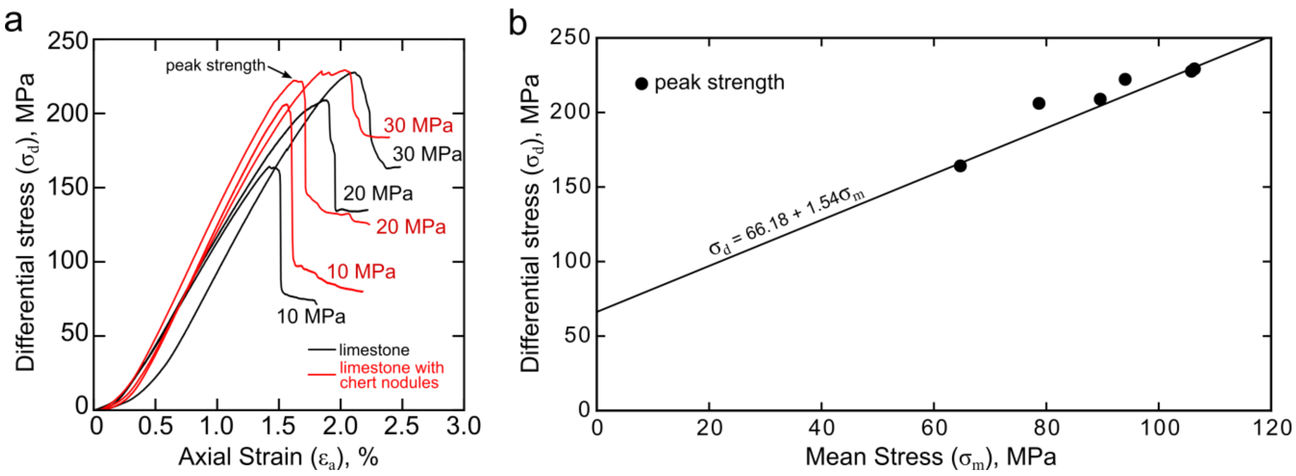

Figure 9. Results from triaxial loading experiments on marly limestones. (a) Evolution of differential stress with increasing axial strain for the tested samples (limestone and limestone with chert) at different confining pressures (P_c = 10-30 MPa). All the experiments show a stress drop after the attainment of a peak value of differential stress. With increasing confining pressure the stress drop is smaller and less sharp. (b) Differential stress at peak strength plotted against the mean stress. Linear regression of peak strength values, excluding the samples where nodules of chert are cut by fractures (10 and 20 MPa), shows M = 1.54 and C = 66.18 (Equation 7).

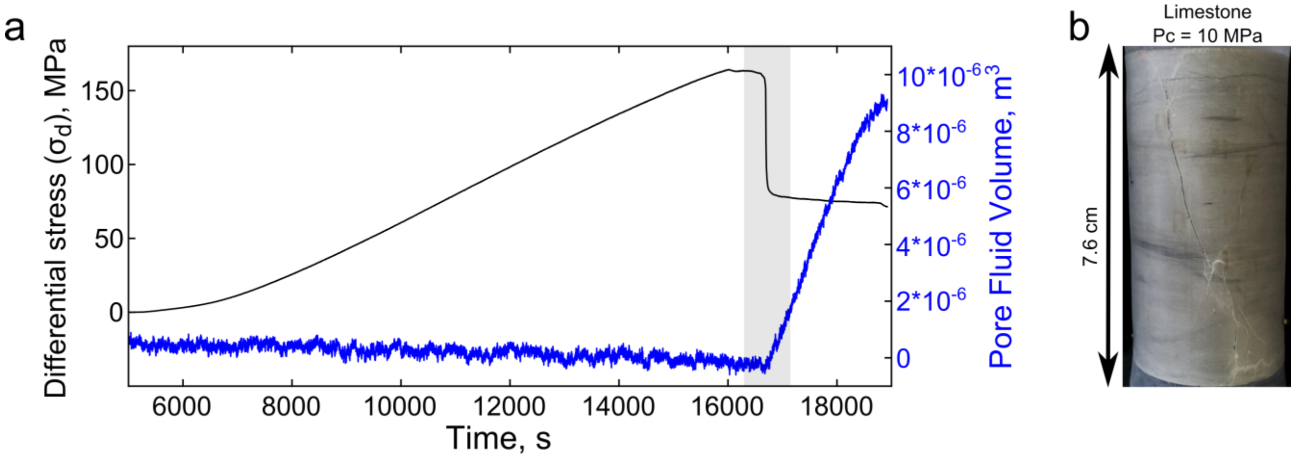

Figure 10. Fracture-enhanced permeability during triaxial experiments at 10 MPa confining pressure. (a) Pore fluid volume remains constant during loading and strongly increases immediately after the stress drop. (b) Failed sample displaying a through-going fracture from the bottom to the top of the rock cylinder, thus explaining the strong increase in pore fluid volume.

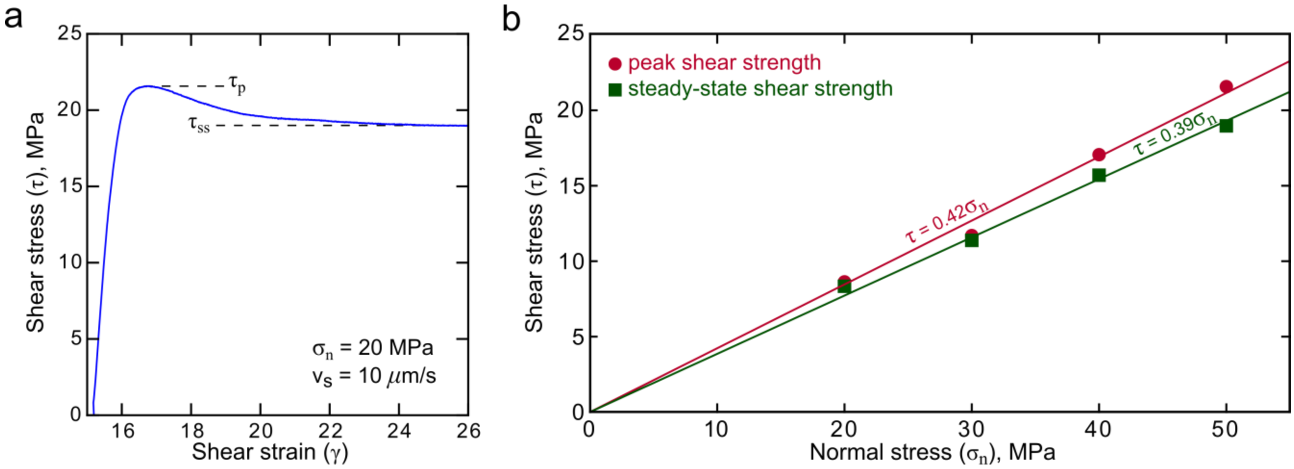

Figure 11. Results from biaxial loading experiments on marls. (a) Shear stress evolution with increasing shear strain. During the experiment, shear stress increases until the attainment of a peak value τ_p and then evolves to a steady-state value τ_{ss}. (b) Shear stress at peak and steady-state plotted against normal stress. The envelope of peak shear stresses results in friction μ_i = 0.42, whereas the envelope of steady-state stresses results in lower friction μ_s = 0.39.

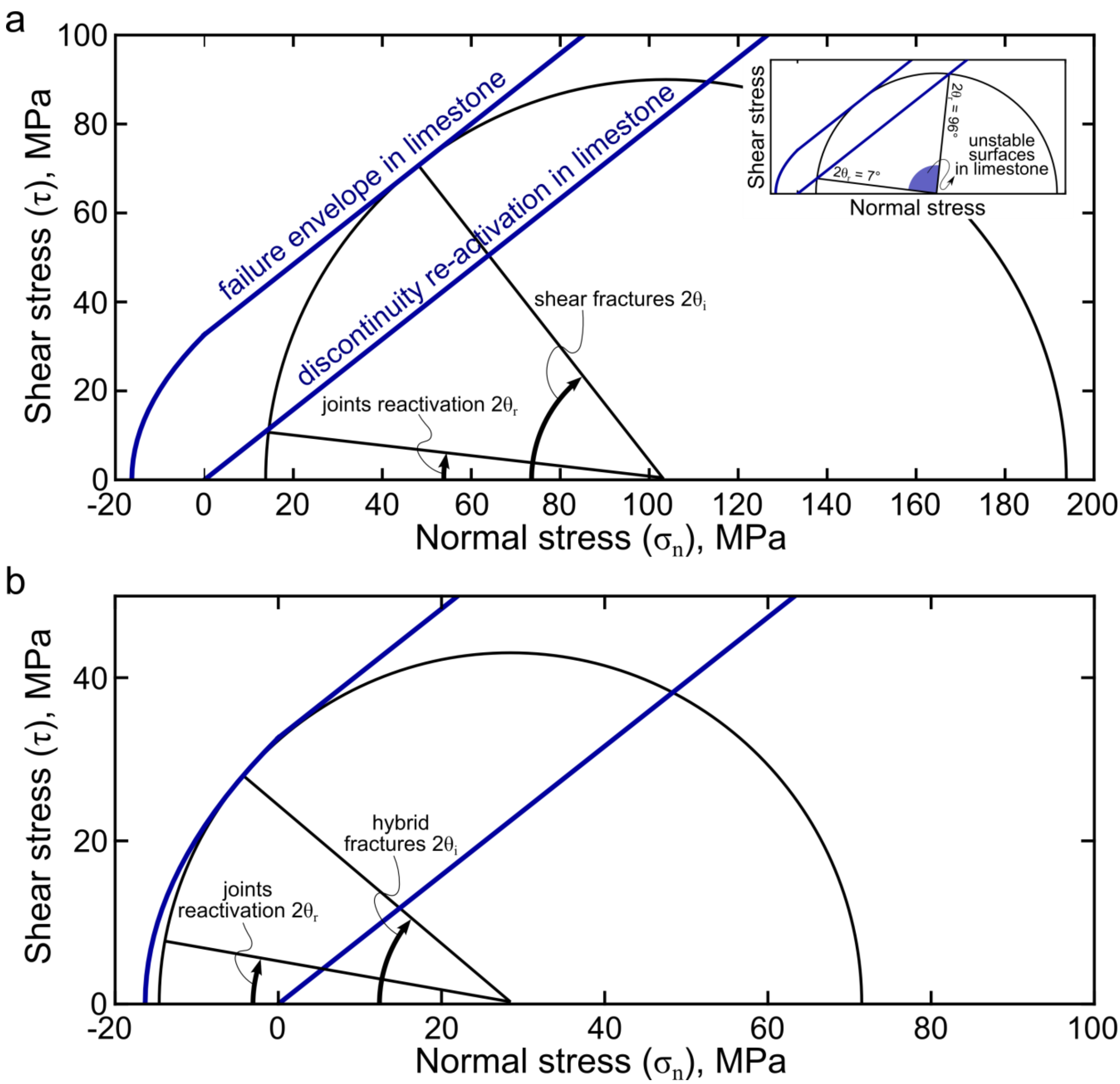

Figure 12. Fault initiation in limestones. We consider the Coulomb failure envelope derived from laboratory experiments for intact limestones and an envelope with the same friction but without cohesion for the reactivation of pre-existing surfaces within limestone. (a) Stress state able to explain the simultaneous initiation of shear fractures and reactivation of joints (discontinuities). In competent layers, when σ_1 and σ_3 are both positive, the initiation of faults with θ_i of ~26° and the reactivation of pre-existing surfaces with θ_r between 3° and 48° can simultaneously occur (cf. also the inset, showing the range of unstable orientations for pre-existing fractures, i.e., $2\theta_r$ = 7 - 96°). In the studied outcrops most of the pre-existing surfaces in calcite-rich layers are joints at low angles,

0 - 20° in Figure 8b, to σ_1. (b) Stress state able to explain the simultaneous initiation of hybrid fractures and reactivation of joints and foliation. In competent layers, when σ_3 is negative, and therefore under small differential stress and high fluid pressure conditions, the initiation of hybrid fractures with θ_i of ~20° and the reactivation of pre-existing surfaces with θ_r between 0° and 58° can simultaneously occur.

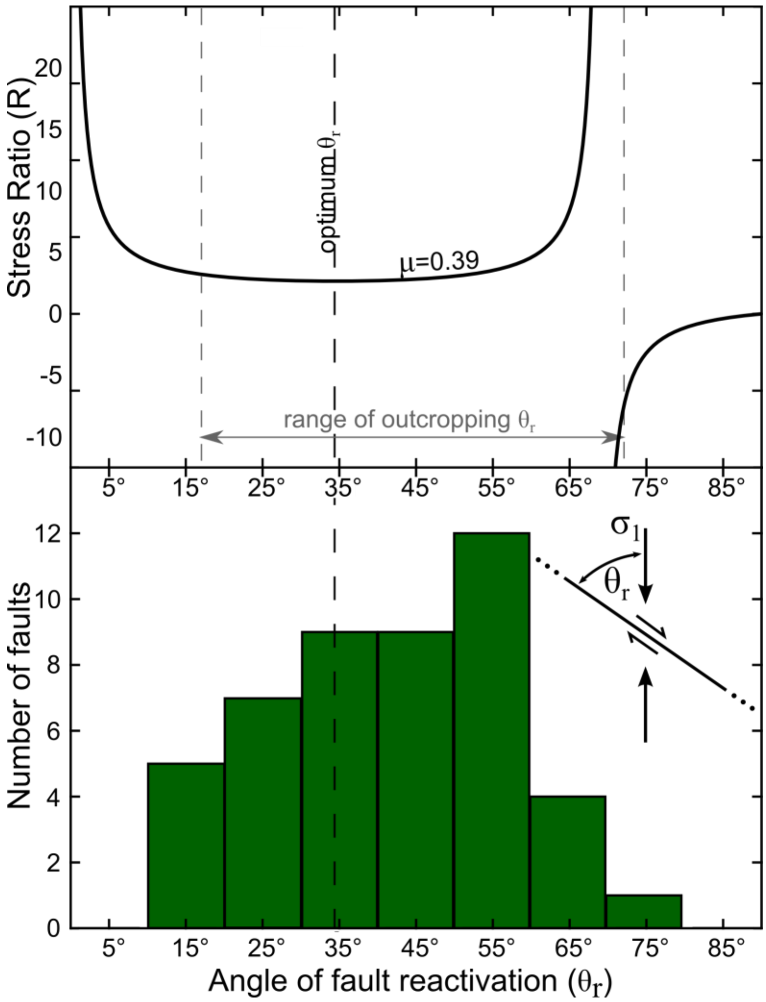

Figure 13. Stress ratio, $R = \sigma_1/\sigma_3$, for frictional reactivation of a cohesionless fault (e.g., *Sibson*, 1985) plotted against the reactivation angle, θ_r, for a friction value of $\mu_s = 0.39$, that is the value obtained from biaxial experiments (see Figure 11b). The distribution of reactivation angles, θ_r, measured for outcropping faults is consistent with a friction value of $\mu_s = 0.39$.